NEUROSCIENCE

Sensory-motor circuit is a therapeutic target for *dystonia musculorum* mice, a model of hereditary sensory and autonomic neuropathy 6

Nozomu Yoshioka[1,2]†, Masayuki Kurose[3,4]‡, Hiromi Sano[5,6,7]‡, Dang Minh Tran[1], Satomi Chiken[5,6], Kazuki Tainaka[8], Kensuke Yamamura[4], Kenta Kobayashi[9], Atsushi Nambu[5,6], Hirohide Takebayashi[1,10]*§

Mutations in Dystonin (*DST*), which encodes cytoskeletal linker proteins, cause hereditary sensory and autonomic neuropathy 6 (HSAN-VI) in humans and the *dystonia musculorum* (*dt*) phenotype in mice; however, the neuronal circuit underlying the HSAN-VI and *dt* phenotype is unresolved. *dt* mice exhibit dystonic movements accompanied by the simultaneous contraction of agonist and antagonist muscles and postnatal lethality. Here, we identified the sensory-motor circuit as a major causative neural circuit using a gene trap system that enables neural circuit-selective inactivation and restoration of *Dst* by Cre-mediated recombination. Sensory neuron–selective *Dst* deletion led to motor impairment, degeneration of proprioceptive sensory neurons, and disruption of the sensory-motor circuit. Restoration of *Dst* expression in sensory neurons using Cre driver mice or a single postnatal injection of Cre-expressing adeno-associated virus ameliorated sensory degeneration and improved abnormal movements. These findings demonstrate that the sensory-motor circuit is involved in the movement disorders in *dt* mice and that the sensory circuit is a therapeutic target for HSAN-VI.

INTRODUCTION

Hereditary neurological diseases usually involve complex abnormalities in neuronal networks, and it is challenging to determine the neuronal circuits that are affected by disease pathogenesis and that have potential as therapeutic targets. Hereditary sensory and autonomic neuropathies (HSANs) are clinically and genetically heterogeneous disorders of the peripheral nervous system (PNS) that are characterized by progressive degeneration of sensory and autonomic neurons (*1*). Mutations in the Dystonin (*DST*) gene, which is also known as bullous pemphigoid antigen 1 (*BPAG1*), cause hereditary sensory and autonomic neuropathy type VI (HSAN-VI). *DST* generates tissue-selective isoforms, DST-a, DST-b, and DST-e (*2*, *3*) that are expressed in neural, muscular, and cutaneous tissues, respectively. DST-a and DST-b are cytoskeletal linker proteins that belong to the plakin family (*4*, *5*). Distinct mutations in the *DST* gene result in a spectrum of symptoms with variations in severity, characteristics, and age of onset, possibly resulting from distinct patterns of DST isoform deficiency (*6*). Although the disease phenotype of HSAN-VI is heterogeneous, sensory and autonomic abnormalities have been commonly described, indicating impairment of the PNS to be crucial for the manifestation of HSAN-VI (*7*–*12*).

Dystonia musculorum (*dt*) mice arose spontaneously and exhibit sensory neuron degeneration in dorsal root ganglia (DRG) at an early postnatal stage and progressive movement disorders, such as ataxia and dystonic movement (*13*). *dt* mice have a loss-of-function mutation in the *Dst* gene (*14*, *15*); therefore, they have been used to investigate the pathogenic mechanisms of HSAN-VI and to develop approaches to treat the disease (*16*, *17*). In addition to neurodegeneration in the PNS, *dt* mice also exhibit abnormalities in the central nervous system (CNS): neurofilament accumulation and neurodegeneration in the spinal cord and brainstem (*17*–*19*) and reduced proliferation of oligodendrocyte progenitor cells (*20*). Therefore, it is not clear to what extent neurodegeneration in the PNS contributes to aspects of the *dt* phenotype, such as motor deficits and postnatal lethality.

Neuronal circuit-selective gene inactivation and restoration of a single allele are promising approaches to determine the neuronal circuit(s) or cell type(s) involved in the pathogenesis of hereditary neurological diseases. However, only a limited number of such studies have been conducted (*21*). Here, we applied a multipurpose *Dst* gene trap allele that enables cell type–selective inactivation and restoration of a target gene through inverting a gene trap cassette by Flip-excision (FLEX) technology (*22*, *23*). Using sensory neuron–selective restoration and inactivation of the *Dst* gene, we demonstrated that impairment of the sensory-motor circuit is responsible for the movement disorder in *dt* mice and that it is a potential target for treating HSAN-VI. The FLEX-mediated multipurpose gene trap system was effective for revealing the pathogenic mechanism of this genetic disease and is a valuable tool for determining causative neuronal circuits in various inherited neurological diseases.

RESULTS

Sensory neuron–selective inactivation or restoration of *Dst* gene

We generated Dst^{Gt} mice harboring the FLEX-mediated multipurpose allele whose gene trap cassette is in the *Dst* locus (Fig. 1A) (*23*). Gene

[1]Division of Neurobiology and Anatomy, Graduate School of Medical and Dental Sciences, Niigata University, Niigata, Japan. [2]Transdisciplinary Research Programs, Niigata University, Niigata, Japan. [3]Department of Physiology, School of Dentistry, Iwate Medical University, Yahaba, Japan. [4]Division of Oral Physiology, Graduate School of Medical and Dental Sciences, Niigata University, Niigata, Japan. [5]Division of System Neurophysiology, National Institute for Physiological Sciences, Okazaki, Japan. [6]Physiological Sciences, SOKENDAI, Okazaki, Japan. [7]Division of Behavioral Neuropharmacology, International Center for Brain Science, Fujita Health University, Toyoake, Japan. [8]Department of System Pathology for Neurological Disorders, Brain Research Institute, Niigata University, Niigata, Japan. [9]Section of Viral Vector Development, National Institute for Physiological Sciences, Okazaki, Japan. [10]Center for Coordination of Research Facilities, Niigata University, Niigata, Japan.
*Corresponding author. Email: takebaya@med.niigata-u.ac.jp
†Present address: Department of Anatomy, School of Life Dentistry at Niigata, The Nippon Dental University, Niigata, Japan.
‡These authors contributed equally to this work.
§Present address: Center for Anatomical Studies, Graduate School of Medicine, Kyoto University, Kyoto, Japan.

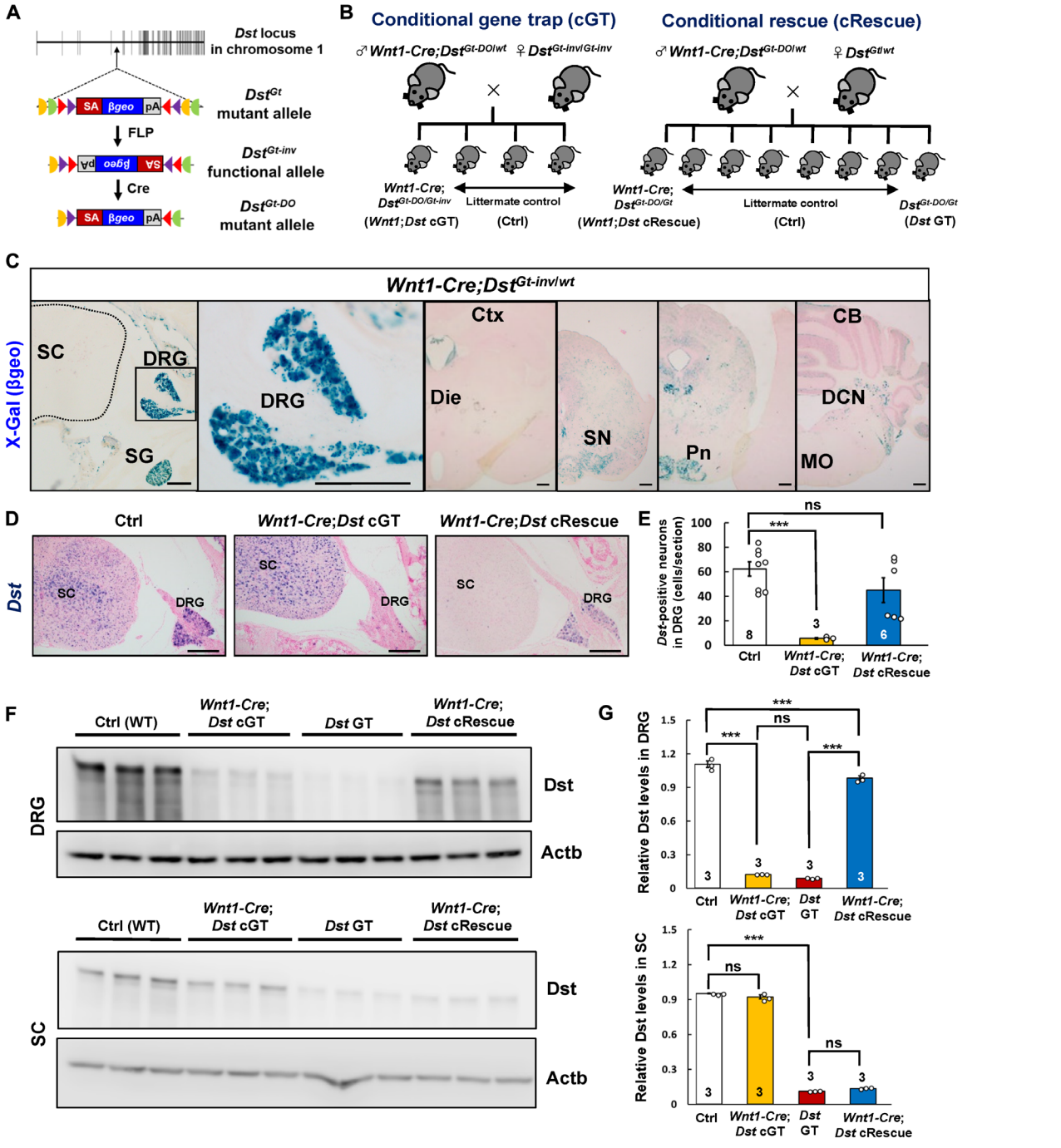

Fig. 1. *Wnt1*-lineage selective deletion and restoration of *Dst* expression. (**A**) The multipurpose gene trap cassette locates in the intron of the *Dst* locus. The gene trap cassette contains splice acceptor (SA) sequence, the reporter gene β*geo*, and poly-A (pA) termination signal. In this FLEX system, the gene trap cassette is flanked by pairs of inversely oriented target sites of FLP recombinase (Frt and F3: half circles) and Cre recombinase (loxP and lox5171: triangles). FLP- or Cre-mediated recombination irreversibly switches mutant Dst^{Gt} allele to functional $Dst^{Gt\text{-}inv}$ allele and functional $Dst^{Gt\text{-}inv}$ allele to mutant $Dst^{Gt\text{-}DO}$ allele. (**B**) Mating scheme to generate *Wnt1-Cre;Dst* cGT and *Wnt1-Cre;Dst* cRescue mice. (**C**) X-gal staining visualized gene trap cassette inversions in 1-month-old *Wnt1-Cre;*$Dst^{Gt\text{-}inv/wt}$ mice. βGeo (blue) was expressed in dorsal root ganglion (DRG) and sympathetic ganglion (SG), while the spinal cord (SC) lacked βgeo expression. In the brain, βgeo was expressed in the cerebellum (CB), pontine nucleus (Pn), and midbrain, while scarcely detected in the cerebral cortex (Ctx), diencephalon (Die), and medulla oblongata (MO). The dotted line indicates the edge of the SC. Boxed area is enlarged to show the DRG. DCN, deep cerebellar nucleus; SN, substantia nigra. (**D**) In situ hybridization in each group at 3 to 4 weeks of age. *Dst* mRNA was lost in DRG neurons of *Wnt1-Cre;Dst* cGT mice but restored in DRG neurons of *Wnt1-Cre;Dst* cRescue mice. (**E**) The number of *Dst*-positive neurons in the DRG [Ctrl ($n = 8$ mice); *Wnt1-Cre;Dst* cGT ($n = 3$); *Wnt1-Cre;Dst* cRescue ($n = 6$)]. (**F**) Western blotting for Dst and β-actin (Actb) in the DRG and SC of 2-week-old mice. (**G**) Quantification of Dst levels normalized to Actb ($n = 3$ mice). Scale bars, 200 μm [(C) and (D)]. Data are presented as mean ± SE. $P > 0.05$ [not significant (ns)] and $^{***}P < 0.005$, using analysis of variance (ANOVA) with Tukey's test in (E) and (G). WT, wild type.

trap cassette disrupts endogenous expression of *Dst* gene and generates a Dst-βgeo fusion protein, which can be detected by X-galactosidase (X-gal) staining. The gene trap cassette is flanked by inversely oriented heterotypic target sites for flippase (FLP) and Cre recombinases. Cre recombination leads to the irreversible switch from the functional $Dst^{Gt\text{-}inv}$ allele to the $Dst^{Gt\text{-}DO}$ mutant allele or from the Dst^{Gt} mutant allele to the functional $Dst^{Gt\text{-}inv}$ allele (Fig. 1A). Dst^{Gt} or $Dst^{Gt\text{-}DO}$ homozygotes and compound heterozygotes of Dst^{Gt} and $Dst^{Gt\text{-}DO}$ exhibit the *dt* phenotype, and we refer these mice as *Dst* GT mice.

To analyze *Dst* functions in the PNS, brainstem, and cerebellum, we used *Wnt1-Cre* transgenic mice (*24*), in which Cre-mediated recombination occurs in neural crest derivatives, including sensory neurons, sympathetic ganglionic neurons, and Schwann cells, and in the developing midbrain-hindbrain (Table 1) (*25*–*27*). For conditional gene trap (cGT) experiments, male *Wnt1-Cre*;$Dst^{Gt\text{-}DO/wt}$ mice were crossed with female $Dst^{Gt\text{-}inv/Gt\text{-}inv}$ mice (Fig. 1B). A quarter of their offspring were *Wnt1-Cre*;*Dst* cGT mice (*Wnt1-Cre*;$Dst^{Gt\text{-}DO/Gt\text{-}inv}$), and we used the mice of the other three genotypes as littermate controls (Ctrl). For conditional rescue (cRescue) experiments, male *Wnt1-Cre*;$Dst^{Gt\text{-}DO/wt}$ mice were crossed with female $Dst^{Gt/wt}$ mice to generate *Wnt1-Cre*;*Dst* cRescue mice (*Wnt1-Cre*;$Dst^{Gt\text{-}DO/Gt}$; Fig. 1B). One-eighth of their offspring were *Wnt1-Cre*;*Dst* cRescue mice, one-eighth were *Dst* GT mice ($Dst^{Gt\text{-}DO/Gt}$, positive control with *dt* phenotype), and the other six genotypes had a wild-type phenotype and were used as Ctrl.

To validate sensory neuron–selective inversions of the gene trap cassette, we performed X-gal staining on sections of *Wnt1-Cre*;$Dst^{Gt\text{-}inv/wt}$ mice because the βgeo reporter is expressed from the recombined $Dst^{Gt\text{-}DO}$ allele in *Wnt1*-lineage cells (Fig. 1C). Most sensory neurons in the DRG and sympathetic ganglionic neurons were labeled by X-gal staining. However, positive signals were very scarce in the spinal cord. The efficiency of Cre-mediated gene trap inversions in DRG neurons was similar at the cervical, thoracic, and lumbar levels (fig. S1A). In cerebellar circuits, positive signals were detected in Purkinje cells, the deep cerebellar nucleus, and the pontine nucleus. In the midbrain, X-gal–labeled cells were also broadly distributed. In contrast to the midbrain-hindbrain, X-gal staining in the forebrain was below detectable levels, including in the cerebral cortex, striatum, and diencephalon. *Dst* is widely expressed in the PNS and CNS (*23*); therefore, these data indicated that Cre-mediated gene trap cassette inversions occurred in *Wnt1*-lineage cells in the PNS and midbrain-hindbrain of *Wnt1-Cre*;$Dst^{Gt\text{-}inv/wt}$ mice.

In situ hybridization confirmed sensory neuron–selective inactivation and restoration of *Dst* expression in *Wnt1-Cre*;*Dst* cGT mice and *Wnt1-Cre*;*Dst* cRescue mice, respectively (Fig. 1, D and E). In Ctrl mice, *Dst* mRNA was detected in DRG sensory neurons and the spinal cord. *Dst* mRNA was selectively deleted in the DRG of *Wnt1-Cre*;*Dst* cGT mice. In contrast, *Dst* mRNA was restored in DRG of *Wnt1-Cre*;*Dst* cRescue mice, while the spinal cord of these mice still lacked *Dst* mRNA. Inactivation and restoration of *Dst* expression exhibited similar trends at the cervical, thoracic, and lumbar levels (fig. S1B). In the brain, *Dst* expression was inactivated in the deep cerebellar nucleus and midbrain of *Wnt1-Cre*;*Dst* cGT mice and restored in the same regions of *Wnt1-Cre*;*Dst* cRescue mice (fig. S2). Dst protein was also examined by Western blotting (Fig. 1, F and G). In *Wnt1-Cre*;*Dst* cGT mice, Dst protein bands were significantly diminished in the DRG but were detected in the spinal cord to the same extent as in Ctrl mice. Conversely, Dst protein was significantly restored in the DRG of *Wnt1-Cre*;*Dst* cRescue mice compared with *Dst* GT mice but remained diminished in the spinal cord of these mice. Therefore, *Dst* mRNA and Dst protein in sensory neurons were deleted and restored in *Wnt1-Cre*;*Dst* cGT mice and *Wnt1-Cre*;*Dst* cRescue mice, respectively.

Phenotypic characterization of *Wnt1-Cre;Dst* cGT mice and *Wnt1-Cre;Dst* cRescue mice

Next, we characterized phenotypes of *Wnt1-Cre*;*Dst* cGT mice and *Wnt1-Cre*;*Dst* cRescue mice. Almost all *Dst* GT mice die until approximately 1 month of age. The life span of *Wnt1-Cre*;*Dst* cRescue mice significantly increased compared with that of *Dst* GT mice. A

Table 1. List of Cre driver mice.

Mouse strain	Targets	MGI	Reference
Wnt1-Cre	PNS	MGI:2386570	(*24*)
	Sensory neurons		
	Sympathetic ganglionic neurons		
	Schwann cells		
	CNS		
	Cerebellum and midbrain		
Avil-Cre	PNS	MGI:4459942	(*34*)
	Sensory neurons		
	Sympathetic ganglionic neurons (after postnatal stage)		
	CNS		
	No target		
En1-Cre	PNS	MGI:2446434	(*38*)
	No target		
	CNS		
	Cerebellum and midbrain		
	Spinal cord interneurons		

total of 68% of *Wnt1-Cre;Dst* cRescue mice survived to more than 100 days, 32% survived to 200 days, and the longest survived to 18 months. *Wnt1-Cre;Dst* cGT mice had a shorter life span than Ctrl mice, and 79% of them died by 200 days of age (Fig. 2A). At 3 weeks of age, body weight gain stopped in *Dst* GT mice. *Wnt1-Cre;Dst* cGT mice also had significantly smaller body sizes than Ctrl mice (Fig. 2B). Body weight gain was also slower in *Wnt1-Cre;Dst* cRescue mice compared with Ctrl mice, and their body size was indistinguishable from that of *Dst* GT mice at 3 weeks of age. This trend of low weight continued with age. These data indicate that loss of *Dst* functions in *Wnt1*-lineage cells is responsible for postnatal lethality and growth arrest in *dt* mice. Differences in the phenotypes of individual cGT or cRescue mice may result from variation in the efficiency and timing of Cre recombination during development. Impaired motor performance and dystonic postures are characteristic phenotypes of *dt* mice (*17*); therefore, we assessed motor performance using the rotarod test (Fig. 2C). *Wnt1-Cre;Dst* cGT mice showed significantly impaired motor performance compared with Ctrl mice as assessed by their ability to stay on an accelerating rotarod. Conversely, *Wnt1-Cre;Dst* cRescue mice showed significantly superior motor performance compared with *Dst* GT mice but did not reach the level of Ctrl mice. The motor impairment in *Wnt1-Cre;Dst* cGT mice and phenotypic rescue in *Wnt1-Cre;Dst* cRescue mice continued in mice over 3 months of age (fig. S3A). Next, we assessed body balance using a balance beam test. Normal Ctrl mice walked smoothly along the beam; however, *Wnt1-Cre;Dst* cGT mice could not kept their balance and immediately fell (movie S1). In sharp contrast, *Wnt1-Cre;Dst* cRescue mice walked smoothly along the beam and reached the goal (movie S1). We also assessed uncoordinated limb movements and dystonic postures in the tail suspension test. During tail suspension, *Wnt1-Cre;Dst* cGT mice showed hindlimb clasping, abnormal extension of both forelimbs and hindlimbs, and sometimes twisting of the trunk, which appeared approximately 10 days after birth (Fig. 2D). In contrast, *Wnt1-Cre;Dst* cRescue mice showed normal posture during tail suspension (Fig. 2D) and rescued from dystonic movement and walked in the cage normally, compared with *Dst* GT mice (movie S2). As a sensory test, the plantar test was performed to evaluate the thermal sensitivity of mice (fig. S3B). Thermal nociceptive function was impaired in *Wnt1-Cre;Dst* cGT mice, and it was rescued in *Wnt1-Cre;Dst* cRescue mice.

Electromyography (EMG) analysis has shown that *Dst* mutant mice exhibit frequent co-contractions of agonist and antagonist muscles (*17*, *23*). EMG recordings were performed from the forelimb triceps and biceps brachii muscles of Ctrl, *Dst* GT, *Wnt1-Cre;Dst* cGT, and *Wnt1-Cre;Dst* cRescue mice in the awake state (Fig. 3A and

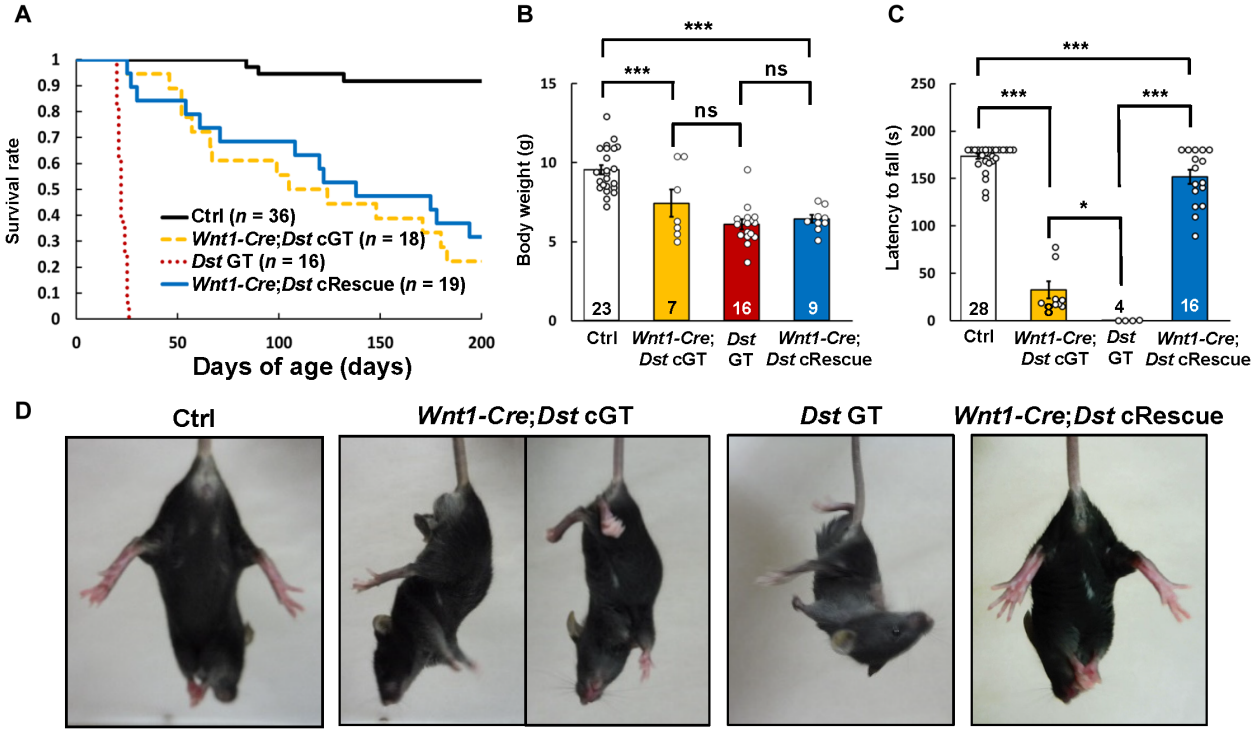

Fig. 2. Phenotypic characterization of *Wnt1-Cre;Dst* cGT mice and *Wnt1-Cre;Dst* cRescue mice. (**A**) Survival curve indicates a shorter life span of *Wnt1-Cre;Dst* cGT mice (yellow dashed line, $n = 18$ mice) than Ctrl mice (black solid line, $n = 36$). *Wnt1-Cre;Dst* cRescue mice (blue solid line, $n = 19$) showed a longer life span than *Dst* GT mice (red dotted line, $n = 16$). (**B**) Body weight (grams) of male mice at 3 weeks of age [Ctrl ($n = 23$ mice); *Wnt1-Cre;Dst* cGT ($n = 7$); *Dst* GT ($n = 16$); *Wnt1-Cre;Dst* cRescue ($n = 9$)]. *Wnt1-Cre;Dst* cGT mice showed significant decrease in body weight compared with Ctrl mice. Body weight of *Wnt1-Cre;Dst* cRescue mice was also light compared with Ctrl mice and not significantly different from *Dst* GT mice. (**C**) In the rotarod test, latency to fall (seconds) was measured to assess motor performance in each group at 3 to 4 weeks of age [Ctrl ($n = 28$ mice); *Wnt1-Cre;Dst* cGT ($n = 8$); *Dst* GT ($n = 4$); *Wnt1-Cre;Dst* cRescue ($n = 16$)]. The motor performance of *Wnt1-Cre;Dst* cGT mice was more impaired than Ctrl mice. The motor performance of *Wnt1-Cre;Dst* cRescue mice was improved than *Dst* GT mice. (**D**) Tail suspension test in each mouse. Ctrl mice maintained a normal posture during tail suspension. *Wnt1-Cre;Dst* cGT mice displayed abnormal postures such as hyperextended and clasped hindlimbs and truncal twists similar to *Dst* GT mice. On the other hand, *Wnt1-Cre;Dst* cRescue mice maintained a normal posture similarly to Ctrl mice. Data are presented as mean ± SE. $P > 0.05$ (ns), $^{*}P < 0.05$, and $^{***}P < 0.005$, using ANOVA with Tukey's test in (B) and (C).

fig. S4, A and B). Co-contractions between the triceps and biceps brachii muscles were more frequently observed in *Dst* GT mice, compared with Ctrl mice and *Wnt1-Cre*;*Dst* cGT mice. In contrast, co-contractions were less frequently observed in *Wnt1-Cre*;*Dst* cRescue mice than *Dst* GT mice (Fig. 3A). We also confirmed these observations by cross-correlograms between the triceps and biceps brachii muscle activities (Fig. 3B). There were no peaks in Ctrl and *Wnt1-Cre*;*Dst* cRescue mice and a high peak at around 0 ms in *Dst* GT mice. In *Wnt1-Cre*;*Dst* cGT mice, there was a low peak at around 0 ms. Therefore, the deletion of *Dst* in *Wnt1*-lineage cells was insufficient to fully reproduce co-contractions observed in *Dst* GT mice. On the other hand, restoring *Dst* expression in *Wnt1*-lineage cells rescued co-contraction between the agonist and antagonist muscles, a hallmark of dystonic movements and postures.

Sensory-motor circuit in *Wnt1-Cre;Dst* cGT and *Wnt1-Cre;Dst* cRescue mice

Sensory neurodegeneration was investigated in *Wnt1-Cre*;*Dst* cGT mice and *Wnt1-Cre*;*Dst* cRescue mice. Neurofilament (NF) accumulation in the CNS and PNS is a pathological hallmark of *dt* mice (*17*–*19*, *28*). Abnormal NF accumulation and induction of activating transcription factor-3 (ATF3), a marker of neural injury, are observed in DRG sensory neurons of *Dst* GT mice throughout the cervical, thoracic, and lumbar levels (Fig. 4, A and C) (*29*). Such pathological alterations also occurred in DRG sensory neurons of *Wnt1-Cre*;*Dst* cGT mice. Meanwhile, NF accumulation and ATF3 expression were scarcely observed in these neurons of *Wnt1-Cre*;*Dst* cRescue mice. In the brain of *Wnt1-Cre*;*Dst* cGT mice, we observed NF accumulations in the cerebellum and midbrain while scarcely observed in their medulla oblongata and cerebral cortex (fig. S5, A and B). In contrast, NF accumulation decreased in the cerebellum and midbrain of *Wnt1-Cre*;*Dst* cRescue mice, compared with *Dst* GT mice (fig. S5, A and B). In sympathetic ganglion neurons of *Wnt1-Cre*;*Dst* cGT mice, ATF3 was up-regulated, whereas ATF3 was not expressed in those of *Wnt1-Cre*;*Dst* cRescue mice (fig. S6, A and B). These data showed that *Dst* loss of function leads to neurodegeneration via cell-autonomous mechanisms. Large-size DRG neurons are more vulnerable than small-size DRG neurons in *dt* mice (*30*). We observed decreased numbers of proprioceptive and mechanosensory neurons in the DRG of *Dst* GT mice, while thermal nociceptive neurons were less affected (fig. S7, A to F). We found that in *Dst* GT mice and *Wnt1-Cre*;*Dst* cGT mice, ATF3 was more frequently expressed in proprioceptive neurons than in thermal nociceptive neurons (fig. S8, A and B). Proprioceptive neurons in the DRG directly form synapses with spinal motor neurons to mediate monosynaptic reflexes. Parvalbumin (PV) and vesicular glutamate transporter 1 (VGluT1) have been used as markers for proprioceptive DRG neurons and proprioceptive synapses on spinal motor neurons, respectively (*31*, *32*). VGluT1 labeling of proprioceptive axon terminals in the anterior horn was significantly decreased in *Dst* GT mice and *Wnt1-Cre*;*Dst* cGT mice compared with that in Ctrl mice (Fig. 4, B and C). Meanwhile, proprioceptive axon terminals were more abundant in *Wnt1-Cre*;*Dst* cRescue mice than *Dst* GT mice (Fig. 4, B and C). In the spinal cord of Ctrl mice and *Wnt1-Cre*;*Dst* cRescue mice, many VGluT1-positive axon terminals contacted with choline acetyltransferase (ChAT)–positive motor neurons, whereas fewer terminals contacted in *Dst* GT mice and *Wnt1-Cre*;*Dst* cGT mice (fig. S9A). *Wnt1-Cre*;*Dst* cGT mice had fewer PV-positive

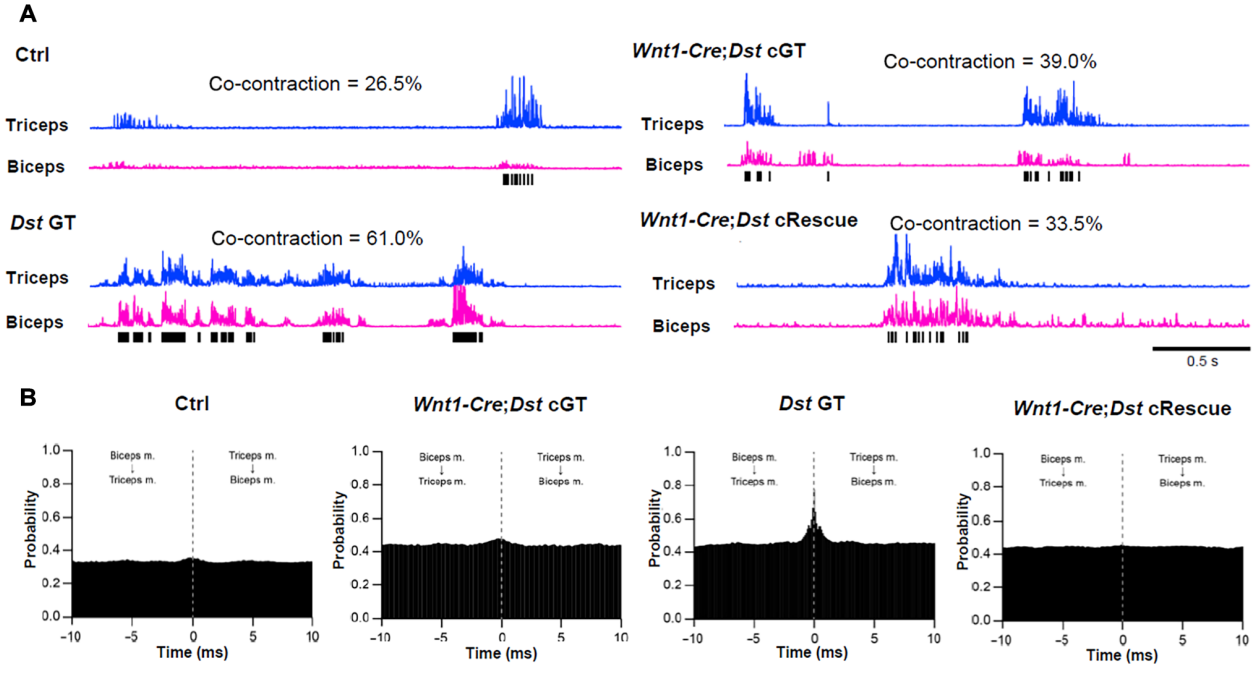

Fig. 3. EMG analysis of simultaneous contractions in *Wnt1-Cre;Dst* cGT mice and *Wnt1-Cre;Dst* cRescue mice. (**A**) Rectified EMG of the triceps (blue) and biceps (magenta) brachii muscles in Ctrl, *Wnt1-Cre*;*Dst* cGT, *Dst* GT, and *Wnt1-Cre*;*Dst* cRescue mice at 6 to 12 weeks of age. Co-contraction between the triceps and biceps brachii muscles (represented by black vertical lines based on Co_{Tri}) was frequently observed in *Dst* GT mice (frequency of co-contraction = 61.0%), less frequently in *Wnt1-Cre*;*Dst* cGT (39.0%) and *Wnt1-Cre*;*Dst* cRescue mice (33.5%), and least frequently in Ctrl mice (26.5%). (**B**) Cross-correlograms between triceps and biceps brachii muscle activity were calculated from rectified EMG of Ctrl, *Wnt1-Cre*;*Dst* cGT, *Dst* GT, and *Wnt1-Cre*;*Dst* cRescue mice. Synchronization between triceps and biceps brachii muscle activity was observed as a hump at around 0 ms in *Dst* GT mice but not in other mice.

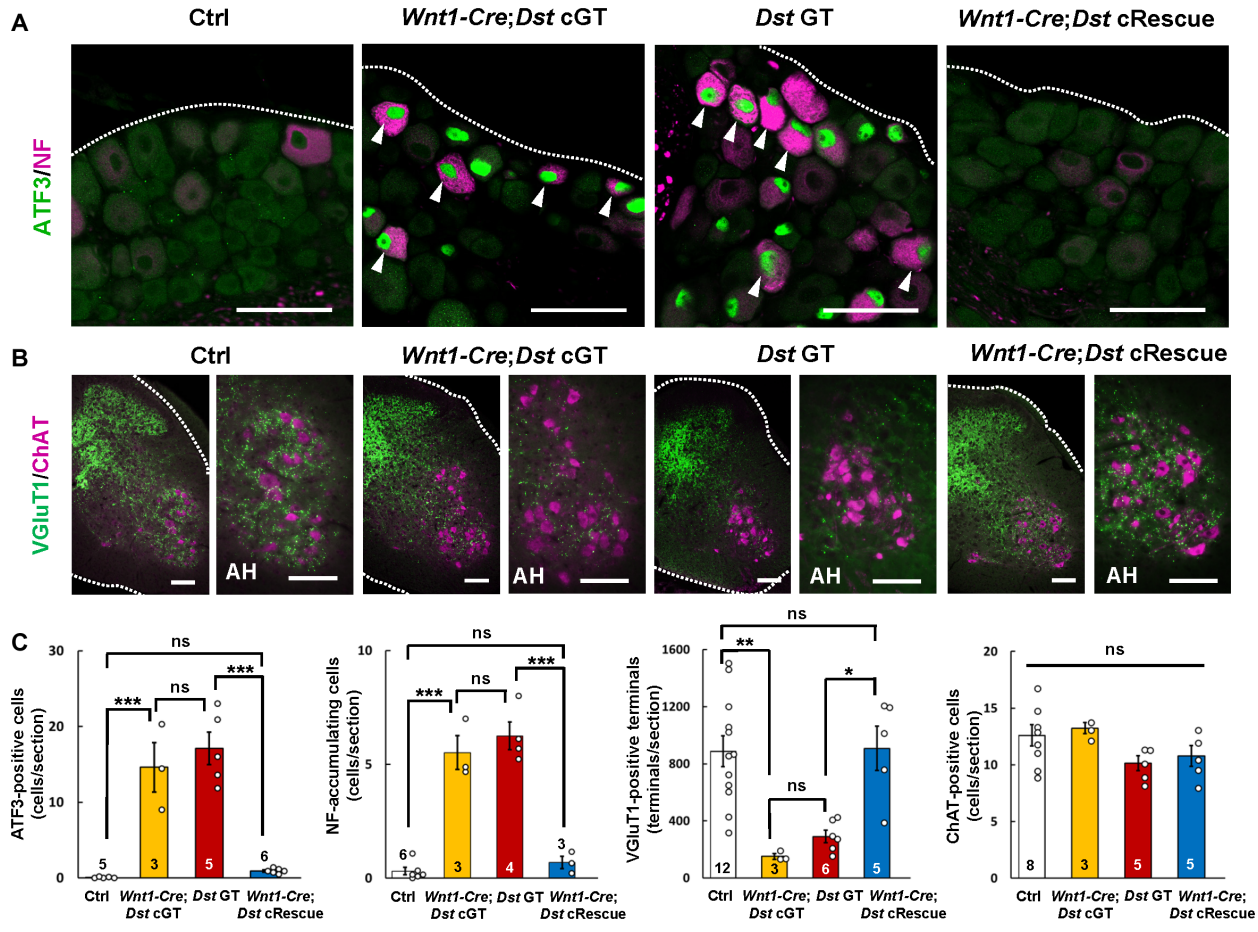

Fig. 4. Histological analysis of sensory-motor circuit in *Wnt1-Cre;Dst* cGT and *Wnt1-Cre;Dst* cRescue mice. (**A**) In *Dst* GT and *Wnt1-Cre;Dst* cGT mice, ATF3 was expressed in some DRG neurons together with neurofilament (NF) accumulation (arrowheads) at 3 to 4 weeks of age. Increases in ATF3 and NF were rarely observed in *Wnt1-Cre;Dst* cRescue mice. The dotted line indicates the edge of the DRG. (**B**) VGluT1-positive axon terminals were observed in the lumbar SC. In the anterior horn (AH), ChAT-positive motor neurons were surrounded by VGluT1-positive axon terminals. There were fewer VGluT1-positive axon terminals in the AH of *Dst* GT and *Wnt1-Cre;Dst* cGT mice than in Ctrl mice, but they were normally distributed in *Wnt1-Cre;Dst* cRescue mice. The dotted line indicates the edge of the SC. (**C**) Quantitative data showed a significant increase in numbers of ATF3-positive cells and NF-accumulating cells in *Dst* GT and *Wnt1-Cre;Dst* cGT mice [ATF3, Ctrl ($n = 5$ mice); *Wnt1-Cre;Dst* cGT ($n = 3$); *Dst* GT ($n = 5$); *Wnt1-Cre;Dst* cRescue ($n = 6$); NF, Ctrl ($n = 6$); *Wnt1-Cre;Dst* cGT ($n = 3$); *Dst* GT ($n = 4$); *Wnt1-Cre;Dst* cRescue ($n = 3$)]. Quantitative data showed a significant decrease in number of VGluT1-positive axon terminals in the AH of *Wnt1-Cre;Dst* cGT mice. VGluT1-positive axon terminals were significantly increased in *Wnt1-Cre;Dst* cRescue mice than *Dst* GT mice [Ctrl ($n = 12$); *Wnt1-Cre;Dst* cGT ($n = 3$); *Dst* GT ($n = 6$); *Wnt1-Cre;Dst* cRescue ($n = 5$)]. The number of ChAT-positive cells was statistically same between groups [Ctrl ($n = 8$); *Wnt1-Cre;Dst* cGT ($n = 3$); *Dst* GT ($n = 5$); *Wnt1-Cre;Dst* cRescue ($n = 5$)]. Scale bars, 50 μm (A) and 200 μm (B). Data are presented as mean ± SE. $P > 0.05$ (ns), $^*P < 0.05$, $^{**}P < 0.01$, and $^{***}P < 0.005$, using ANOVA with Tukey's test in (C).

proprioceptive neurons and *Trkb*-positive mechanosensory neurons compared with Ctrl mice, while *Wnt1-Cre;Dst* cRescue and Ctrl mice had comparable numbers (fig. S6, C to F). No significant differences in the number of ChAT-positive motor neurons were observed between Ctrl, *Wnt1-Cre;Dst* cGT, *Dst* GT, and *Wnt1-Cre;Dst* cRescue mice (Fig. 4, B and C).

Next, we performed electrophysiological analyses to assess functional changes in the sensory-motor circuit. We stimulated the tibial nerve and recorded EMG in the plantar muscle. An M response, a direct response, is produced by motor neuron activation. A Hoffmann reflex (H-reflex) is produced by a spinal cord pathway consisting of group Ia afferents from the muscle spindles and the motor neurons (Fig. 5A). In Ctrl mice, the M response and H-reflex sequentially occurred following stimulation. In *Wnt1-Cre;Dst* cGT mice, attenuated H-reflex was recorded with delay (Fig. 5B and fig. S10). The H-reflex was rescued in *Wnt1-Cre;Dst* cRescue mice than in *Dst* GT mice (Fig. 5B and fig. S10). The frequency of successful H-reflexes was lower in *Dst* GT and *Wnt1-Cre;Dst* cGT mice than in Ctrl mice. The H/M amplitude ratio (H response maximum amplitude/M response maximum amplitude) in *Dst* GT and *Wnt1-Cre;Dst* cGT mice was significantly reduced compared with that in Ctrl mice (Fig. 5C). The latencies of both the M response and H-reflex in *Dst* GT mice and *Wnt1-Cre;Dst* cGT mice were significantly longer than in Ctrl mice, while *Wnt1-Cre;Dst* cRescue mice showed normal M response and H-reflex latency (Fig. 5C). These data demonstrated reduced amplitude and delayed response of the H-reflex in *Wnt1-Cre;Dst* cGT mice. In contrast, the H-reflex in *Wnt1-Cre;Dst* cRescue mice showed normal amplitude and latency. These data indicate that the proprioceptive feedback circuit is morphologically and functionally disrupted or rescued following inactivation or restoration of *Dst* expression in sensory neurons,

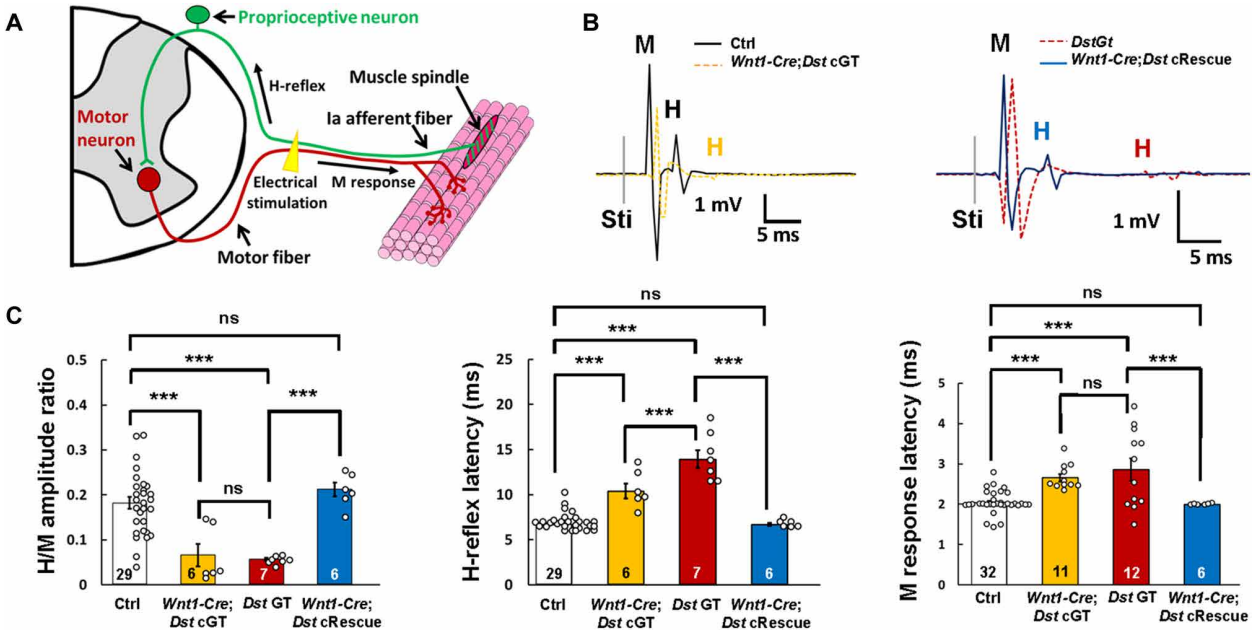

Fig. 5. Functional analysis of the sensory-motor circuit in *Wnt1-Cre;Dst* cGT and *Wnt1-Cre;Dst* cRescue mice. (**A**) A diagram of the H-reflex mediated by proprioceptive sensory neurons and motor neurons. The M response was evoked by electronic stimulation of motor fibers in the tibial nerve of mice. The H-reflex is transmitted via Ia afferent fibers derived from proprioceptive neurons. (**B**) Representative EMG images of M response and H-reflex. In Ctrl mice, electrical stimulation (Sti) evoked M response and H-reflex sequentially (black solid line). In *Wnt1-Cre;Dst* cGT mice, H-reflex was attenuated and delayed (yellow dashed line). In *Wnt1-Cre;Dst* cRescue mice, stimulation normally induced H-reflex (blue solid line), whereas it was attenuated and delayed in *Dst* GT mice (red dashed line). (**C**) Quantitative data of H/M amplitude ratio, H-reflex latency (milliseconds), and M response latency (milliseconds) in each mouse group at 3 to 4 weeks of age. H/M amplitude ratio was significantly decreased in *Dst* GT mice and *Wnt1-Cre;Dst* cGT mice compared to Ctrl mice, whereas *Wnt1-Cre;Dst* cRescue mice had a normal level of H/M amplitude ratio as in Ctrl mice [H/M amplitude ratio and H-reflex latency, Ctrl ($n = 29$); *Wnt1-Cre;Dst* cGT ($n = 6$); *Dst* GT ($n = 7$); *Wnt1-Cre;Dst* cRescue ($n = 6$); sample sizes are numbers of successful evocation of H-reflex]. The latencies of H-reflex and M response in *Dst* Gt mice and *Wnt1-Cre;Dst* cGT mice were significantly longer than in Ctrl mice, while latencies of both responses in *Wnt1-Cre;Dst* cRescue were statistically same as in Ctrl mice [M response latency, Ctrl ($n = 32$); *Wnt1-Cre;Dst* cGT ($n = 11$); *Dst* GT ($n = 12$); *Wnt1-Cre;Dst* cRescue ($n = 6$); sample sizes are numbers of measurement of M response]. Data are presented as mean ± SE. $P > 0.05$ (ns) and ***$P < 0.005$, using ANOVA with Tukey's test in (C).

respectively. We therefore consider that loss of *Dst* function in the sensory circuit leads to disruption of proprioceptive sensory feedback and movement disorders.

Manipulation of *Dst* separately in the sensory-motor circuit and cerebellar circuit

Our data suggested that disruption to the sensory-motor circuit underlies the dystonic movements in *dt* mice. However, Cre-mediated recombination also occurred in the cerebellar circuits of *Wnt1-Cre;Dst*$^{Gt\text{-}inv/wt}$ mice (Fig. 1C). Therefore, it is still possible that inactivation of *Dst* in cerebellar circuits also contributes to abnormal movements in *dt* mice. *Dst* expression was separately manipulated in PNS neurons and cerebellar circuits using *Advillin* (*Avil*)–*Cre* mice and *En1-Cre* mice to distinguish involvement of the PNS and cerebellum (Table 1). *Avil-Cre* mice produce Cre-mediated recombination in PNS neurons, including sensory neurons of DRG and trigeminal ganglia after the late developmental stage but rarely in the brain and spinal cord (*33*). We therefore used *Avil-Cre* knock-in mice, which have been used for PNS neuron–specific gene manipulations (*33*–*37*). In *Avil-Cre;Dst*$^{Gt\text{-}inv/wt}$ mice, Cre-mediated gene trap switching was restricted to DRG neurons and was not observed in cerebellar circuits (fig. S11A). *Dst* mRNA was significantly decreased in DRG neurons of *Avil-Cre;Dst*$^{Gt\text{-}DO/Gt\text{-}inv}$ (*Avil-Cre;Dst* cGT) mice, whereas *Dst* expression was restored in DRG neurons of *Avil-Cre;Dst*$^{Gt\text{-}DO/Gt}$ (*Avil-Cre;Dst* cRescue) mice (fig. S11, B and E). *En1-Cre* knock-in mice have been used to manipulate *Dst* expression in the cerebellum and spinal interneurons (*38*, *39*). We confirmed inversion of the gene trap cassette in cerebellar circuits, including in Purkinje cells, deep cerebellar nucleus neurons, and the pontine nucleus in *En1-Cre;Dst*$^{Gt\text{-}inv/wt}$ mice, while gene trap inversion did not occur in DRG neurons (fig. S11A). Although *En1-Cre* mice label large population of spinal interneurons (*39*), we did not observe X-gal–positive cells in the *En1-Cre;Dst*$^{Gt\text{-}inv/wt}$ spinal cord. Therefore, it seems that *En1*-lineage spinal interneurons do not express Dst. Moreover, *Dst* expression in DRG neurons was not inactivated in *En1-Cre;Dst* cGT mice and not restored in *En1-Cre;Dst* cRescue mice (fig. S11, B and E).

Avil-Cre;Dst cGT mice exhibited sensory neurodegeneration accompanied by NF accumulation and ATF3 induction, whereas *Avil-Cre;Dst* cRescue mice exhibited an ameliorated phenotype (fig. S11, C to E). *Avil-Cre;Dst* cGT mice did not display decrease of *Dst* mRNA and NF accumulation in the cerebellum/midbrain regions, unlike *Wnt1-Cre;Dst* cGT mice (fig. S12, A and B). *En1-Cre;Dst* cGT mice did not exhibit NF accumulation or ATF3 induction in DRG sensory neurons (fig. S11, C to E). However, decrease of *Dst* mRNA and NF accumulation were observed in the cerebellum/midbrain regions of *En1-Cre;Dst* cGT mice, as in *Wnt1-Cre;Dst* cGT mice (fig. S12, A and B). *Avil-Cre;Dst* cGT mice exhibited hindlimb clasping in the tail suspension test, whereas *Avil-Cre;Dst* cRescue mice could maintain normal posture (Fig. 6A). Freely moving *Avil-Cre;Dst* cRescue mice did not display dystonic movements (movie S3). *Avil-Cre;Dst* cGT mice and *Avil-Cre;Dst* cRescue

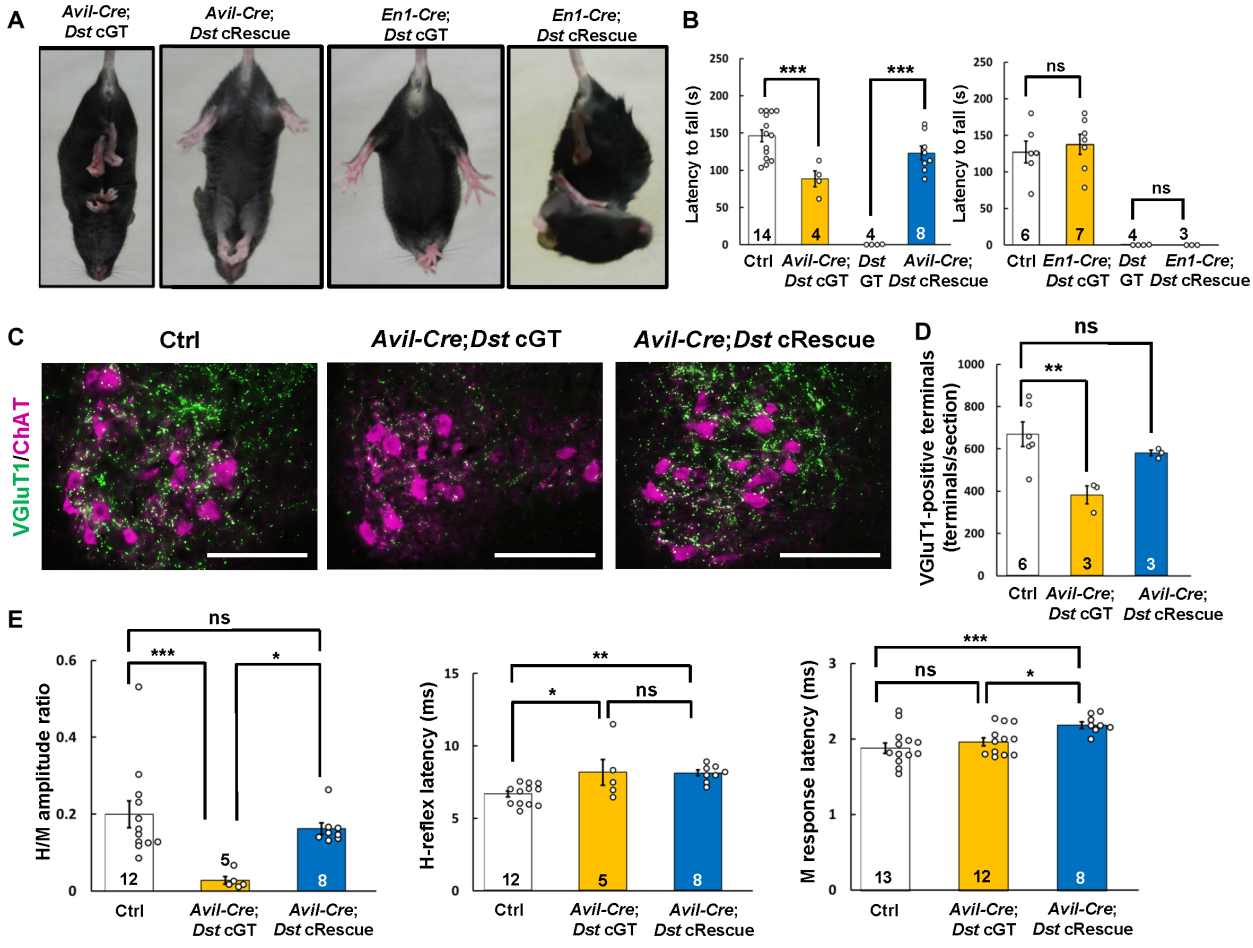

Fig. 6. Manipulation of *Dst* expression separately in sensory neurons and cerebellar circuits. (**A**) During tail suspension, *Avil-Cre;Dst* cGT mice showed hindlimb clasping at 3 to 4 weeks of age, while *Avil-Cre;Dst* cRescue mice maintained normal postures. *En1-Cre;Dst* cGT and *En1-Cre;Dst* cRescue mice neither developed nor rescued abnormal postures, respectively. (**B**) In a rotarod test, *Avil-Cre;Dst* cGT mice displayed shorter latency to fall (seconds) than Ctrl. *Avil-Cre;Dst* cRescue mice performed better than *Dst* GT mice [Ctrl ($n = 14$ mice); *Avil-Cre;Dst* cGT ($n = 4$); *Dst* GT ($n = 4$); *Avil-Cre;Dst* cRescue ($n = 8$)]. *En1-Cre;Dst* cGT and *En1-Cre;Dst* cRescue mice showed no differences compared to Ctrl and *Dst* GT mice, respectively [Ctrl ($n = 6$); *En1-Cre;Dst* cGT ($n = 7$); *Dst* GT ($n = 4$); *En1-Cre;Dst* cRescue ($n = 3$)]. (**C**) In the lumbar SC of each group at 3 months old, VGluT1-labeled terminals were decreased in *Avil-Cre;Dst* cGT mice than Ctrl but normal in *Avil-Cre;Dst* cRescue mice. (**D**) Quantitative data on numbers of VGluT1-positive terminals [Ctrl ($n = 6$ mice); *Avil-Cre;Dst* cGT ($n = 3$); *Avil-Cre;Dst* cRescue ($n = 3$)]. (**E**) Quantification of electrophysiological data in mice at 3 months of age. H/M amplitude ratio was reduced in *Avil-Cre;Dst* cGT mice than Ctrl but normal in *Avil-Cre;Dst* cRescue mice [H/M amplitude ratio and H-reflex latency, Ctrl ($n = 12$); *Avil-Cre;Dst* cGT ($n = 5$); *Avil-Cre;Dst* cRescue ($n = 8$); sample sizes are numbers of successful evocation of H-reflex]. *Avil-Cre;Dst* cRescue mice show delayed M response and H-reflex [M response latency, Ctrl ($n = 13$); *Avil-Cre;Dst* cGT ($n = 12$); *Avil-Cre;Dst* cRescue ($n = 8$); sample sizes are numbers of measurement of M response]. Scale bars, 100 μm (C). Data are presented as mean ± SE. $P > 0.05$ (ns), $^*P < 0.05$, $^{**}P < 0.01$, and $^{***}P < 0.005$, using ANOVA with Tukey's test in (B), (D), and (E).

mice showed impaired and rescued motor performance, respectively, as assessed by the rotarod test (Fig. 6B). On the other hand, postures and motor performance were not impaired in *En1-Cre;Dst* cGT mice and not rescued in *En1-Cre;Dst* cRescue mice (Fig. 6, A and B, and movie S4). The number of VGluT1-labeled proprioceptive synapses around motor neurons was decreased in *Avil-Cre;Dst* cGT mice, whereas *Avil-Cre;Dst* cRescue mice had abundant proprioceptive synapses, similar to Ctrl mice (Fig. 6, C and D, and fig. S9B). The number of PV-positive proprioceptive neurons also decreased in *Avil-Cre;Dst* cGT mice than Ctrl mice, whereas *Avil-Cre;Dst* cRescue mice had similar number of these neurons as Ctrl mice (fig. S13, A and B). In *Avil-Cre;Dst* cGT mice, some proprioceptive neurons expressed ATF3 (fig. S8, A and B). Electrophysiological analysis also demonstrated that the H/M amplitude ratio was small in *Avil-Cre;Dst* cGT mice and that latency of the H-reflex in *Avil-Cre;Dst* cGT mice was significantly longer than that in Ctrl mice (Fig. 6E). Unlike *Wnt1-Cre;Dst* cGT mice, *Avil-Cre;Dst* cGT mice did not exhibit prolongation of the M response latency (Fig. 6E). Conversely, the H/M amplitude ratio of *Avil-Cre;Dst* cRescue mice was normal, while the latencies of the M response and H-reflex did not rescue compared with Ctrl mice (Fig. 6E). These data indicate that disruption of the sensory-motor circuit and not the cerebellar circuit is responsible for dystonic movements in *dt* mice.

Treatment of *Dst*^{Gt} mice with a postnatal AAV injection

Intraperitoneal administration of AAV9 vectors allows efficient gene transfer to DRG neurons in neonatal mice (*40*). Therefore, we attempted to ameliorate the movement disorder in *Dst*^{Gt} homozygous mice through systemic delivery of an adeno-associated virus (AAV).

AAV9–green fluorescent protein (GFP) or AAV9-Cre was intraperitoneally administered to Dst^{Gt} homozygous mice with an ICR background at an early postnatal stage (Fig. 7A). After tissue clearing using clear unobstructed brain/body imaging cocktails and computational analysis (CUBIC), we observed the projecting axons of GFP-labeled DRG neurons in the dorsal funiculus (Fig. 7B). In transverse sections of the spinal cord, GFP-labeled axons were predominantly observed in the dorsal horn, with some located in the anterior horn (Fig. 7C). We also observed GFP-labeled axons in the medullar oblongata where dorsal funiculus and trigeminal nerve fibers project and sparse GFP-labeled cells in other brain regions (movie S5). The life span of the Dst^{Gt} homozygous mice was approximately 3 to 4 weeks, and a single injection of AAV9-Cre extended their life span: Approximately half of these mice survived for 4 months, and some (~10%) survived for more than 10 months (Fig. 7D). Dystonic movements and motor performance were improved in the AAV9-Cre–treated Dst^{Gt} homozygous mice (Fig. 7E and movie S6), and footfalls were reduced on the horizontal ladder floor (Fig. 7F). It should be noted that motor performance of AAV9-Cre–treated mice gradually worsened at 2 months after treatment, while their motor symptom still seemed to be milder than nontreated Dst^{Gt} mice (movie S7). *Dst* expression was restored in the DRG neurons of the AAV9-Cre–treated Dst^{Gt} mice, while *Dst* mRNA was not detected in AAV9-GFP–treated Dst^{Gt} mice (Fig. 7, G and H). Treatment with AAV9-Cre ameliorated sensory neurodegeneration and increased numbers of proprioceptive neurons and proprioceptive synapses around motor neurons (Fig. 8, A and B, and fig. S9C). The H/M amplitude ratio and the H-reflex latency were rescued in Dst^{Gt} homozygous mice treated with AAV9-Cre compared with nontreated Dst^{Gt} homozygous mice (Fig. 8C). Two months after AAV9-Cre injection, ATF3 was slightly increased in the DRG of Dst^{Gt} homozygous mice (fig. S14). However, PV-positive proprioceptive neurons were observed as normal, and some PV-positive neurons expressed ATF3 after 2 months of AAV treatment (fig. S14). Therefore, we considered that the decline in motor performance after 2 months of AAV-Cre treatment is related to dysfunction of proprioceptive neurons rather than neuronal loss.

DISCUSSION

In this study, we used a FLEX-mediated multipurpose gene trap system that enables tissue-selective inactivation and restoration of *Dst* expression to demonstrate that disruption of the sensory-motor circuit is involved in the movement disorder of *dt* mice. *Dt* mice exhibit dystonic movements and postures accompanied by synchronized muscle

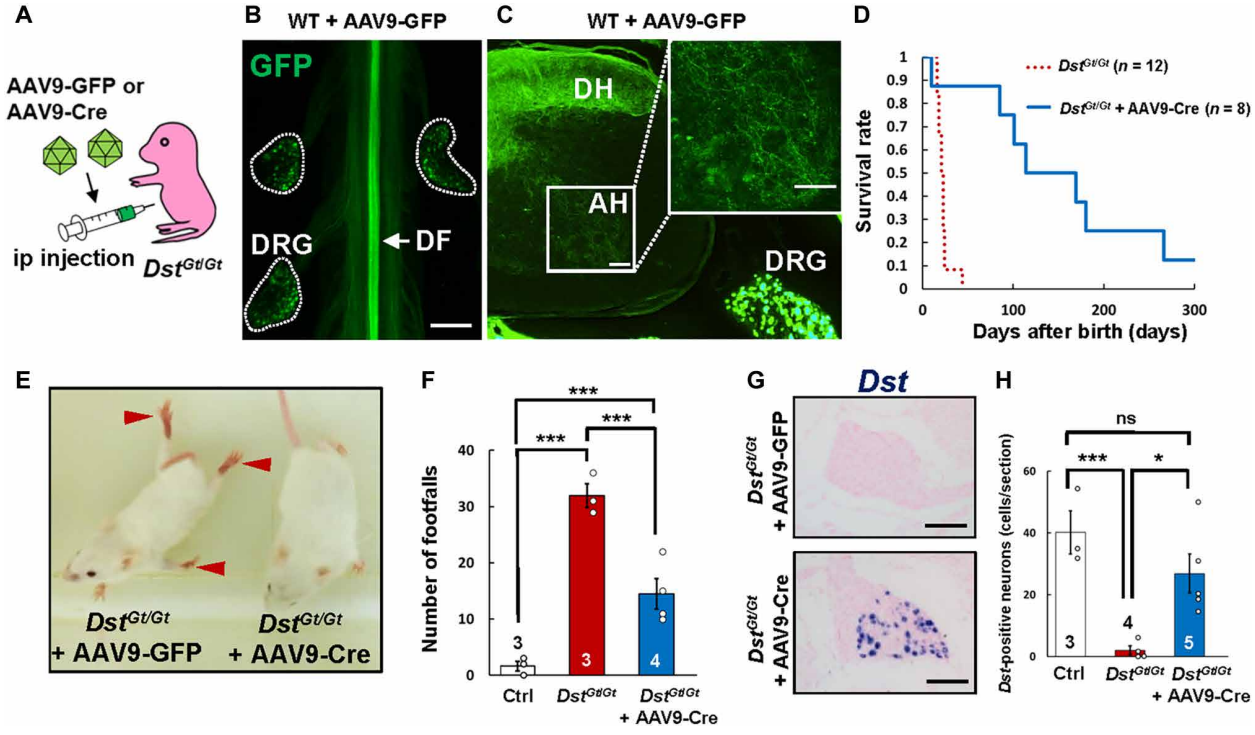

Fig. 7. Presymptomatic restoration of *Dst* expression using viral vectors rescued disease phenotypes. (**A**) Intraperitoneal (ip) injection of AAV9-Cre or AAV9-GFP into neonatal $Dst^{Gt/Gt}$ mice. (**B**) A reconstructed transparent SC image from AAV9-GFP–injected wild-type mice at 2 months of age. GFP labeled the DRG and sensory tract in the dorsal funiculus (DF, arrow). The dotted line indicates the edge of DRG. (**C**) GFP-labeled axons are distributed in the dorsal horn (DH). In the AH, axons of proprioceptive neurons were also labeled with GFP. (**D**) The survival curve indicates a life extension of AAV9-Cre–treated $Dst^{Gt/Gt}$ mice (blue solid line, $n = 8$ mice) compared with $Dst^{Gt/Gt}$ mice (red dashed line, $n = 12$). (**E**) AAV9-GFP–treated $Dst^{Gt/Gt}$ mice exhibited twist movements with hyperextension of forelimbs and hindlimbs (arrowheads). AAV9-Cre–treated $Dst^{Gt/Gt}$ mice showed normal posture 3 weeks after injection. (**F**) Motor performance was assessed by counting number of footfalls on the horizontal ladder floor. Impaired motor performance of $Dst^{Gt/Gt}$ mice was represented with many footfalls compared with Ctrl mice. AAV9-Cre treatment significantly improved motor performance of $Dst^{Gt/Gt}$ mice at 3 weeks of age while not reaching the Ctrl level [Ctrl ($n = 3$ mice); $Dst^{Gt/Gt}$ ($n = 3$); $Dst^{Gt/Gt}$ + AAV9-Cre ($n = 4$)]. (**G**) In situ hybridization image in the DRG from each group at 3 weeks of age. *Dst* mRNA was detected in DRG neurons of $Dst^{Gt/Gt}$ mice injected with AAV9-Cre, but *Dst* mRNA was diminished in DRG neurons of $Dst^{Gt/Gt}$ mice injected with AAV9-GFP. (**H**) Quantitative data on numbers of *Dst*-positive neurons in the DRG [Ctrl ($n = 3$ mice); $Dst^{Gt/Gt}$ ($n = 4$); $Dst^{Gt/Gt}$ + AAV9-Cre ($n = 5$)]. Scale bars, 500 μm (B), 50 μm (C), and 100 μm (G). Data are presented as mean ± SE. $P > 0.05$ (ns), $^{*}P < 0.05$, and $^{***}P < 0.005$, using ANOVA with Tukey's test in (F) and (H).

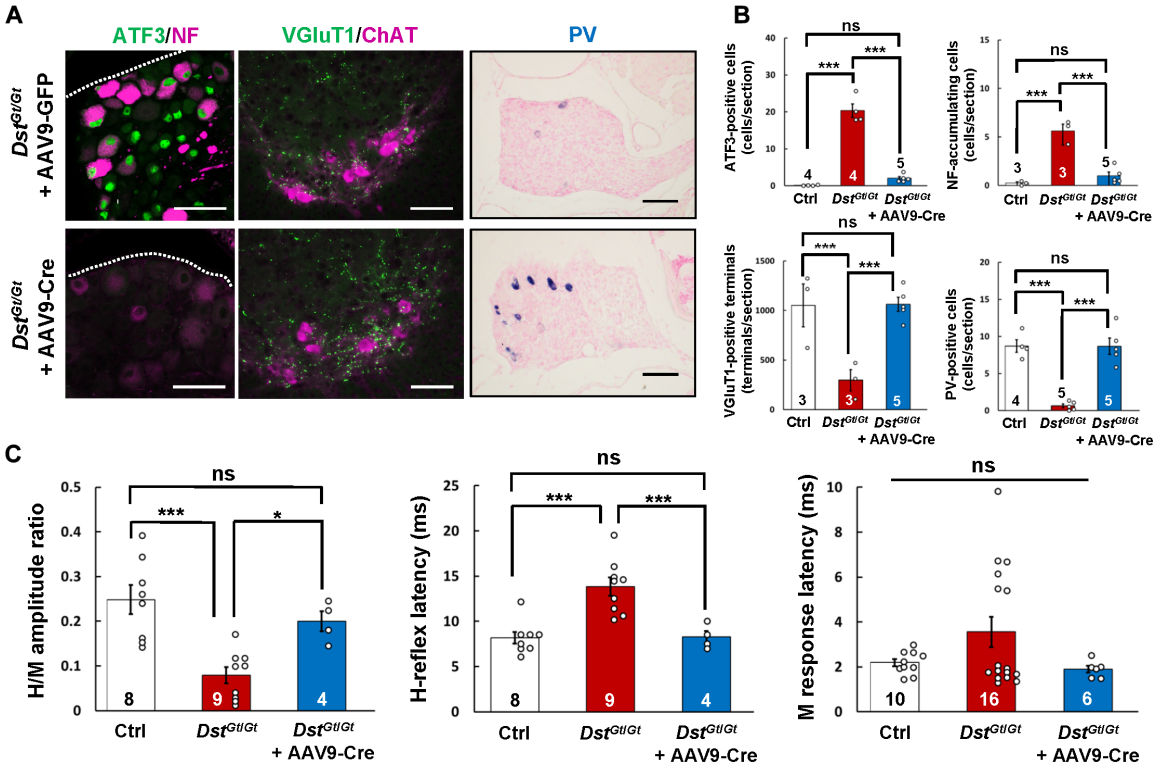

Fig. 8. Presymptomatic treatment with AAV rescued the sensory-motor circuit of *Dst*^{Gt} mice. (**A**) Histological analysis of neurodegeneration in each group at 3 weeks of age. In DRG of *Dst*$^{Gt/Gt}$ mice injected with AAV9-GFP, ATF3 and NF accumulation was abundantly observed, and there were few VGluT1-positive axon terminals around motor neurons in the AH of lumbar SC. In DRG of *Dst*$^{Gt/Gt}$ mice injected with AAV9-Cre, ATF3 and NF accumulation was scarcely observed, and VGluT1-positive axon terminals were abundant. PV-positive proprioceptive neurons were few in the DRG of *Dst*$^{Gt/Gt}$ mice injected with AAV9-GFP while normally observed in *Dst*$^{Gt/Gt}$ mice injected with AAV9-Cre. (**B**) Quantification of numbers of ATF3-positive cells [Ctrl ($n = 4$ mice); *Dst*$^{Gt/Gt}$ ($n = 4$); *Dst*$^{Gt/Gt}$ + AAV9-Cre ($n = 5$)], NF-accumulating cells [Ctrl ($n = 3$); *Dst*$^{Gt/Gt}$ ($n = 3$); *Dst*$^{Gt/Gt}$ + AAV9-Cre ($n = 5$)], PV-positive cells [Ctrl ($n = 4$); *Dst*$^{Gt/Gt}$ ($n = 5$); *Dst*$^{Gt/Gt}$ + AAV9-Cre ($n = 5$)], and VGluT1-positive axon terminals [Ctrl ($n = 3$); *Dst*$^{Gt/Gt}$ ($n = 3$); *Dst*$^{Gt/Gt}$ + AAV9-Cre ($n = 5$)]. (**C**) Quantification of electrophysiological data in mice at 2 to 3 weeks of age. H/M amplitude ratio and H-reflex latency in *Dst*$^{Gt/Gt}$ mice were rescued by injection with AAV9-Cre. [H/M amplitude ratio and H-reflex latency, Ctrl ($n = 8$); *Dst*$^{Gt/Gt}$ ($n = 9$); *Dst*$^{Gt/Gt}$ + AAV9-Cre ($n = 4$); sample sizes are numbers of successful evocation of H-reflex; M response latency, $n = 10$ Ctrl; $n = 16$ *Dst*$^{Gt/Gt}$; $n = 6$ *Dst*$^{Gt/Gt}$ + AAV9-Cre; sample sizes are numbers of measurement of M response]. Scale bars, 50 μm (A). Data are presented as mean ± SE. $P > 0.05$ (ns), $^{*}P < 0.05$, and $^{***}P < 0.005$, using ANOVA with Tukey's test in (B) and (C).

activities between agonist and antagonist muscles. Inactivation of *Dst* in PNS neurons leads to disruption of sensory-motor circuits and impaired motor performance. Conversely, restoring *Dst* in PNS neurons ameliorated sensory neurodegeneration, suppressed synchronized muscle activities, rescued dystonic movements, and extended life span. The therapeutic effects of postnatal *Dst* restoration by a single injection of AAV-Cre advocate the efficacy of gene therapy for HSAN-VI. Overall, we have identified the sensory circuit as a therapeutic target of HSAN-VI after birth.

The FLEX-mediated multipurpose gene trap system useful for elucidating pathogenesis

The FLEX-mediated multipurpose gene trap system in a single allele is a useful experimental system to investigate gene function (*22*, *41*). Here, we applied this technology to elucidate pathogenic mechanisms and therapeutic targets of the inherited neurological disease HSAN-VI. The short life span of *dt* mice makes it challenging to analyze the mechanisms that underlie the *dt* phenotype. However, sensory neuron–selective inactivation of *Dst* reproduced the disease phenotypes of *dt* mice and circumvented postnatal lethality. Therefore, cGT is helpful for determining neural circuits and cell types involved in disease pathogenesis and for developing animal models that can avoid lethality when loss-of-function mutations in a gene directly cause lethality. However, the specificity and efficiency of Cre recombination need to be considered when interpreting experimental results. For example, *Wnt1-Cre;Dst* cGT mice exhibited more severe symptoms than *Avil-Cre;Dst* cGT mice. Such phenotypic differences in cGT mice might be caused by spatiotemporal differences in Cre recombination between *Wnt1-Cre* and *Avil-Cre* mice (*42*). *Wnt1-Cre*–mediated recombination occurs in a wide range of neural crest derivatives, including sensory neurons, sympathetic ganglionic neurons, and Schwann cells (*27*), whereas *Avil-Cre*–mediated recombination occurs in sensory neurons and postganglionic neurons of the autonomic nervous system (*34*, *35*). In the present results, the M response latency was prolonged in *Wnt1-Cre;Dst* cGT mice, while it was unchanged in *Avil-Cre;Dst* cGT mice. This difference is probably due to differential recombination in Schwann cells. We have previously demonstrated the significance of Dst in Schwann cells for maintaining myelin sheaths in the PNS (*43*). Conditional *Dst* deletion in Schwann cells using a *P0-Cre* transgene resulted in late-onset neuropathy with prolongation of M response latency. This suggests that lack of Dst in sensory neurons, not in Schwann cells, is the primary cause of early

postnatal neurodegeneration and abnormal movements in *dt* mice. On the other hand, Dst in Schwann cells is essential for the maintenance of myelin sheaths and normal nerve conduction in the PNS at the adult stage. Patients with HSAN-VI suffer from autonomic dysfunction and sensory neuropathy (*7*–*11*). Neuronal degeneration in the autonomic nervous system has been reported in *dt* mice (*44*, *45*). We are now investigating the significance of autonomic dysfunctions in *dt* mice. Abnormalities of multiple PNS cell types may be associated with the pathogenesis of HSAN-VI.

The PNS as a therapeutic target for *dt* mice and HSAN-VI

Here, we investigated the target to ameliorate the *dt* phenotype through conditional restoration of *Dst* in several tissues. *Dst* cRescue with *Wnt1-Cre* and *Avil-Cre* but not *En1-Cre* improved motor performance and prolonged life span, indicating that the *Wnt1* and *Avil* lineages of PNS neurons rather than the cerebellum/midbrain are therapeutic targets of *dt* mice. Therefore, PNS neurons are a potential therapeutic target for *dt* mice, a mouse model of HSAN-VI. Our results are also supported by the previous study showing that transgenic expression of *Dst* under a neuron-specific promoter partially rescues the *dt* phenotype (*16*). Notably, a single administration of AAV-Cre at the early postnatal stage improved the survival and functional rescue of the sensory circuit, leading to improved motor symptoms and prolonged life span. These results indicate that the sensory circuit of *dt* mice is a target for gene therapy after birth. Previous studies have proposed gene therapy using viral vectors as a therapeutic strategy for sensory neuropathy (*46*, *47*). A single dose of AAV encoding the survival motor neuron protein has been successfully used to treat patients with spinal muscular atrophy, an inherited motor neuron disease (*48*). The success of postnatal AAV therapy in *dt* mice shows that the same strategy has promise for treating HSAN-VI and other hereditary neuropathies. However, the size limit of an exogenous gene (5 kb) in AAV makes it difficult to insert the large *DST-a* gene (18 kb) into the AAV genome for gene delivery. There is, however, the possibility of applying genome editing methods to enable treatment using AAV injection (*49*, *50*). HSAN-VI presents a spectrum of symptoms due to the complexity of the *DST* gene, which generates tissue-selective isoforms, which need to be considered in therapy development (*3*, *6*). In addition to the neural DST-a isoform associated with HSAN-VI, there is an epidermal DST-e isoform involved in epidermolysis bullosa simplex (*51*, *52*). Furthermore, we also found late-onset protein aggregate myopathy and cardiomyopathy in *Dst-b* isoform–specific mutant mice (*29*). Life-span recovery by *Dst* cRescue in the PNS with *Wnt1-Cre* and AAV9-Cre was incomplete. Thus, defects in Dst isoforms other than PNS may also be associated with the disease phenotype of *dt* mice. When considering the treatment of these *DST* disorders, the location of each *DST* mutation and the target tissue expressing the mutated *DST* isoform must be considered.

Causative neuronal circuits in dystonic movement disorders

As the name suggests, *dt* mice exhibit dystonic movements with co-contractions between agonist and antagonist muscles. The neural circuit mechanisms of dystonia remain unclear. Previous studies of mouse genetic models of *DYT1-TorsinA* (*TOR1A*), a causative gene for hereditary dystonia, and manipulation of cerebellar circuits have shown that neuronal circuits in the cerebellum and striatum are involved in dystonia (*53*–*59*). The dystonia-causal *Tor1a* mutation *Dyt1ΔE* impairs the formation of inhibitory synapses against proprioceptive afferent synapses on motor neurons (*60*), but their involvement in motor deficits remains to be elucidated. In some mouse models, disruption of proprioception causes ataxia and abnormal posture (*61*–*64*). The recent report of conditional deletion of *Tor1a* in the spinal cord and DRG describes impaired monosynaptic reflexes in the spinal cord and recapitulates early-onset generalized torsional dystonia (*65*). The lack of *Tor1a* in the spinal cord was also considered to contribute to dystonia because DRG-specific *Tor1a* deletion alone does not reproduce dystonia. Together, the neural circuits responsible for dystonia are probably diverse and unclear.

Traditionally, dystonia has been considered a disorder of the basal ganglia, but previous studies suggest that dystonia is a network disorder involving a wide range of sensory-motor regions. In the present study, we demonstrated that normalization of the sensory-motor circuit suppressed co-contraction between agonist and antagonist muscles and rescued dystonic movements and postures in *dt* mice. Furthermore, we found that *Dst* deletion in sensory neurons caused disruption of the sensory-motor circuit, ataxia, and twisting movements during tail suspension but did not fully reproduce co-contractions. These results indicate that disruption of the proprioceptive circuit contributes to dystonic movement in *dt* mice; however, disruption of other circuits is also necessary to fully reproduce dystonia with co-contraction. Dystonic movements caused by sensory loss resulting from spinal cord or PNS damage are called pseudo-dystonia to distinguish them from dystonia associated with basal ganglia abnormalities (*66*). Although the contributions of sensory circuit abnormalities to dystonia are still to be elucidated, our study adds to the current understanding of the neural circuit mechanisms of dystonia.

MATERIALS AND METHODS

Animals

We used $Dst^{Gt(E182H05)}$ mice (Dst^{Gt}; mouse genome informatics number, MGI:3917429) (*23*) derived from the embryonic stem (ES) clone (ID: E182H05) obtained from German Genetrap Consortium (*22*). Dst^{Gt} mice were crossed with several Cre-driver mice (Table 1) including neural crest and midbrain/cerebellum-selective *Wnt1-Cre* transgenic mice [$H2az2^{Tg(Wnt1-cre)11Rth}$; MGI:2386570] (*24*), sensory neuron–selective *Avil-Cre* mice [$Avil^{tm2(cre)Fawa}$; MGI:4459942] (*34*), and midbrain/cerebellum-selective *En1-Cre* mice [$En1^{tm2(cre)Wrst}$; MGI:2446434] (*38*). The Dst^{Gt} line was backcrossed to C57BL/6NCrj (Charles River Japan Inc.) or ICR (SLC Japan) for at least 10 generations. The inbred C57BL/6NCrj strains were used for mouse genetics. Because ICR mice have larger body size and produce more offspring than C57BL/6NCrj mice, ICR strains were used for infections with viral vectors. The functional $Dst^{Gt\text{-}inv}$ allele (MGI:7423689) was inverted from Dst^{Gt} allele by FLP recombinase, and mutant $Dst^{Gt\text{-}DO}$ allele (MGI:7423690) was inverted from $Dst^{Gt\text{-}inv}$ allele by Cre recombinase (*23*). Mutant mice of Dst^{Gt}, $Dst^{Gt\text{-}inv}$, and $Dst^{Gt\text{-}DO}$ were maintained in each line. Since heterozygotes of Dst^{Gt} or $Dst^{Gt\text{-}DO}$ are fertile, homozygotes of Dst^{Gt} or $Dst^{Gt\text{-}DO}$ were obtained by the heterozygous mating. To perform Cre-mediated conditional inactivation or restoration of the *Dst* expression, gene trap mice harboring multipurpose *Dst* alleles were crossed with each Cre driver mouse. Male and female mice were analyzed in this study, but only male mice were used for body weight comparisons. The animal experiments were approved by the Internal Review Board of Niigata University (permit numbers: SA00521 and SA00621) and the Institutional Animal Care and Use Committee of the National Institutes of Natural Sciences (21A014), and the guidelines of Niigata University Animal Care and Use Committee

were followed. Mice were maintained at 23° ± 3°C, 50 ± 10% humidity, and 12-hour light/dark cycle with food and water available ad libitum. Humane endpoints were applied as per veterinary recommendation, and the criteria used to determine when mice should be euthanized included severe dehydration, immobility, and desertion by feeding mother.

X-gal staining

The X-gal staining was performed as described previously (*23*). Tissues were fixed with a mixture of 2% paraformaldehyde (PFA) and 0.2% glutaraldehyde, immersed in the fixative overnight, and transferred to 20% sucrose in 20 mM phosphate-buffered saline (PBS; pH 7.4) until they sank. The tissues were frozen in liquid nitrogen and embedded in Tissue-Tek OCT compound (Sakura Finetek Japan, Tokyo, Japan), and 16-μm-thick sections were cut on a cryostat (Leica CM1850 UV; Leica, Wetzlar, Germany; HM525 NX; Thermo Fisher Scientific). Sections were washed for 10 min in PBS and incubated with X-gal staining solution {5 mM $K_4[Fe(CN)_6]$, 5 mM $K_3[Fe(CN)_6]$, 20 mM Tris-HCl (pH 7.3), 2 mM $MgCl_2$, 0.2% NP-40, 0.1% sodium deoxycholate, and 0.1% X-gal in PBS} at 37°C for 3 days. We used tissues from littermate $Dst^{Gt\text{-}inv/+}$ mice as negative controls.

Tissue preparations and in situ hybridization

For tissue preparation, mice were euthanized with an intraperitoneal injection of pentobarbital sodium (100 mg/kg body weight) and then perfused with 4% PFA in 0.1 M phosphate-buffered (PB) solution (pH 7.4) by cardiac perfusion with 0.01 M PBS followed by ice-cold 4% PFA in 0.1 M PB (pH 7.4). Dissected tissues were immersed in the same fixative overnight. For cutting the spinal cord and DRG sections, the specimens were rinsed with water for 10 min and decalcified in Morse solution (135-17071; Wako, Osaka, Japan) overnight. Tissues were dehydrated through an ascending series of ethanol and xylene and then embedded in paraffin (P3683; Paraplast Plus; Sigma-Aldrich, St. Louis, USA). Consecutive 10-μm-thick paraffin sections were cut on a rotary microtome (HM325; Thermo Fisher Scientific), mounted on Matsunami Adhesive Silane (MAS)-coated glass slides (Matsunami Glass, Osaka, Japan), and air-dried on a hot plate overnight at 37°C.

In situ hybridization was performed on paraffin sections described in the previous study (*67*). The following probes were used: mouse *Dst-plakin* (GenBank accession number: NM_001276764, nucleotides 2185 to 3396), mouse PV (also known as *Pvalb*, NM_013645, nucleotides 92 to 885), rat *TrkA* (a gift from K. Abe, accession number M85214, nucleotides 80 to 427), mouse *Trkb* (a gift from S. Nakamura) (*68*), rat *TrkC* (a gift from K. Abe, accession number L14445, nucleotides 1 to 311), mouse *Vglut1* (also known as *Slc17a7*, NM_182993, nucleotides 618 to 1266) (*69*), mouse *CGRP* (also known as *Calca*, GenBank accession number, NM_001289444, nucleotides 567 to 914), mouse *Galectin-1* (also known as *Lgals1*, GenBank accession number, NM_008495, nucleotides 12 to 769), and mouse *Trpm8* (GenBank accession number, NM_134252, nucleotides 2151 to 2968).

Immunohistochemistry

Analyses of immunohistochemistry (IHC) were performed on paraffin sections. For IHC, deparaffinized sections were treated with microwave irradiation in 10 mM citric acid buffer (pH 6.0) for 5 min and incubated overnight at 4°C with the following primary antibodies: rabbit polyclonal anti-ATF3 antibody (1:2000; Santa Cruz Biotechnology; sc-188), rabbit polyclonal anti-VGluT1 antibody (1:1000; Frontier Institute, Hokkaido, Japan; Rb-Af500), goat polyclonal anti-VGluT1 antibody (1:1000; Frontier Institute; Go-Af310), goat polyclonal anti-ChAT antibody (1:500; Millipore; AB144P), guinea pig polyclonal anti-CGRP antibody (1:300; Frontier Institute; GP-Af280), mouse monoclonal anti-neurofilament-M antibody (1:500; 1C8) (*70*), and mouse monoclonal anti-PV antibody (1:1000; Sigma-Aldrich; PARV-19, P3088), diluted in 0.1 M PBS with 0.01% Triton X-100 (PBST) containing 0.5% skim milk. Sections were then incubated in horseradish peroxidase–conjugated secondary antibody (1:200; Medical & Biological Laboratories (MBL), Nagoya, Japan) diluted in PBST containing 0.5% skim milk for 60 min at 37°C. Between each step, sections were rinsed in PBST for 15 min. After rinsing sections in distilled water, immunoreaction was visualized in 50 mM Tris buffer (pH 7.4) containing 0.01% diaminobenzidine tetrahydrochloride and 0.01% hydrogen peroxide at 37°C for 5 min. Sections were dehydrated through ethanol-xylene and coverslipped with Bioleit (23-1002; Okenshoji, Tokyo, Japan). For immunofluorescent staining, sections were incubated in mixtures of Alexa Fluor 488– or Alexa Fluor 594–conjugated secondary antibodies (1:200; Invitrogen, CA) for 60 min at 37°C. Mounted sections were air-dried and coverslipped. Digital images were taken with a microscope (BX53; Olympus, Tokyo, Japan) equipped with a digital camera (DP74, Olympus) and a confocal laser scanning microscopy (FV-1200, Olympus). Tag image file format (TIFF) files were processed with Photoshop software (Adobe, San Jose, USA).

Western blotting

Western blotting was performed as previously described (*52*). Frozen spinal cord and DRG were homogenized in ice-cold homogenization buffer [0.32 M sucrose, 5 mM EDTA, 10 mM Tris-HCl (pH 7.4), and phosphatase inhibitor cocktail tablet; Roche] and centrifuged at 4500 rpm for 10 min at 4°C, and the supernatants were collected. The protein concentration was determined using the bicinchoninic acid Protein Assay Reagent (Thermo Fisher Scientific). Lysates were mixed with an equal volume of 2× SDS sample buffer [125 mM Tris-HCl (pH 6.8), 4% SDS, 20% glycerol, and 0.002% bromophenol blue] for a final protein concentration of 0.5 to 1 μg/μl and denatured in the presence of 100 mM dithiothreitol at 100°C for 5 min. SDS–polyacrylamide gel electrophoresis was performed with 5 to 10 μg per lane on 5 to 20% gradient gels (197-15011; SuperSep Ace; FUJIFILM Wako Pure Chemical Corporation, Osaka, Japan) running at 10 to 20 mA for 150 min. The gels were blotted onto an Immobilon-P transfer membrane (Millipore, Billerica, MA, USA). After blocking with 10% skim milk for 3 hours, blotted membranes were incubated with the following primary antibodies: rabbit polyclonal anti-Dst antibody (gifted from R. K. Liem) (*71*) which recognizes the plakin domain of Dst and mouse monoclonal anti–β-actin antibody (1:2000; AB_2223041; clone C4, Merck Millipore). Each of the first antibodies was incubated overnight at 4°C. Then, membranes were incubated with peroxidase-conjugated secondary antibodies for 1 hour at room temperature: anti-rabbit immunoglobulin G (IgG) (1:2000; AB_2099233; catalog no. 7074, Cell Signaling Technology, Beverly, MA, USA) or anti-mouse IgG (1:2000; AB_330924; catalog no. 7076, Cell Signaling Technology). Tris-buffered saline [10 mM Tris-HCl (pH 7.5) and 150 mM NaCl] containing 0.1% Tween 20 and 10% skim milk was used to dilute primary and secondary antibodies, and Tris-buffered saline containing 0.1% Tween 20 was used as the washing buffer. Immunoreactions were visualized by enhanced chemiluminescence (GE Healthcare, Piscataway Township, NJ, USA).

Images were acquired, and signal intensities from bands were determined using a luminescence image analyzer (C-Digit, LI-COR, Lincoln, NE, USA).

Behavioral tests

We performed behavioral tests to evaluate motor performance. In the rotarod test (O'Hara & Co.) (*29*), we measured the latency to fall from the rotating rod (30-mm diameter with an acceleration from 10 to 150 rpm). Each trial was conducted for 3 min. In each mouse, two trials were conducted in a day. In the balance beam test, we evaluate the ability of balance and motor performance (O'Hara & Co.) (*72*). Mice were placed on the end of the 1-m beam (10 mm in diameter) resting 50 cm above the table on two poles and containing a block box placed at the other end of the beam as the finish point. In the horizontal ladder test, mice were placed on the metal rungs (3 mm in diameter with 9-mm distance), and then footfalls of the hindlimbs from the ladder floor were counted from the side view.

The severity of dystonia was assessed in a home cage using locomotor disability scores, as previously described (*16*). The scores were graded as follows: D0 (no motor abnormalities), D1 (slightly slowed or abnormal motor behavior, no dystonia), D2 (mild impairment, sometimes limited ambulation, dystonic postures when disturbed), D3 (moderate impairment, frequent spontaneous dystonic postures), D4 (severe impairment, sustained dystonic postures, and limited ambulation), and D5 (prolonged immobility in dystonic postures).

To evaluate thermal sensitivity, we performed a plantar test (O'Hara & Co.). Each mouse was placed on a glass floor and surrounded with a clear plastic cage. Radiant thermal stimuli were applied to a hind paw from under a glass floor, and the latency of paw withdrawal was measured. The level of heat stimulation was kept constant throughout the test among the animals.

Measurement of co-contraction by EMG

EMG recordings from the triceps and biceps brachii muscles of the forelimb were performed in the awake state as previously described (*17*, *23*). For EMG recordings from *Dst* GT mice, these mice were prolonged by intraperitoneal injection with 5% glucose in saline and rearing with MeiBalance mini in agarose (Meiji, Tokyo, Japan). Briefly, mice were anesthetized with isoflurane (1.0 to 1.5%) and fixed in a stereotaxic apparatus. A small U-frame head holder was mounted on the mouse's head as described previously (*23*, *73*, *74*). Then, the EMG recording electrodes (bipolar wire electrodes; tip distance, 1 to 2 mm) made of 140-mm-diameter Teflon-coated seven-stranded stainless steel wire (A-M Systems) were implanted in the bellies of the triceps and biceps brachii muscles of the forelimb. The wires were passed subcutaneously and soldered to connectors attached to the U-frame. After recovery from the surgery, the awake mouse was positioned painlessly in the stereotaxic apparatus using the U-frame head holder. The EMG signals from the triceps and biceps brachii muscles were amplified (×1000), filtered (0.25 to 1.5 kHz), and archived to a computer at a sampling rate of 10 kHz. The EMG was recorded for 20 s when mice moved their limbs intermittently. The EMG was rectified, and co-contraction of the triceps and biceps brachii muscles was analyzed by the following two methods using Igor software (WaveMetrics). (i) EMG was resampled at 1 kHz (1-ms bin, decimation by averaging). Local maximal points (peaks) of rectified EMG were marked during significant changes (>mean + 1.65 SD calculated from 20-s recording) in the triceps and biceps brachii muscles and counted (Tri and Bi, respectively). If a local maximal point of triceps brachii EMG coincided with 3 bins (3 ms) centered at a local maximal point of biceps brachii EMG, then it was considered as co-contraction defined from the triceps brachii muscle (Co_{Tri}). The similar calculation was performed starting from the biceps brachii muscle (Co_{Bi}). Percentage of co-contraction was calculated as $(Co_{Tri}/Tri + Co_{Bi}/Bi)/2 \times 100$. (ii) Cross-correlograms of rectified EMG were constructed between the triceps and biceps brachii muscles.

Measurement of H-reflex

H-reflex was measured as previously described (*43*). Mice at 2 weeks to 3 months of age were anesthetized by an intraperitoneal application of ketamine (60 mg/kg) and xylazine (10 mg/kg) during all electrophysiological experiments. Depth of anesthesia was checked repeatedly throughout the experiment by pinching the paws. Ketamine/xylazine was additionally administrated when a withdrawal reflex was elicited. For H-reflex recordings, the tibial nerve was exposed and kept moist in a mineral oil pool made with skin flaps as described previously (*75*, *76*). The nerve was hooked to a custom-made bipolar stimulating electrode (Unique Medical, Tokyo, Japan). A pair of needle electrodes were inserted in the interosseous muscles of the hindpaw for EMG recordings. The signals were fed into a computer equipped with a Cambridge Electronic Design (CED) Power 1401 board and analysis software (Spike 2 ver 6.17; Cambridge Electronic Design Ltd., Cambridge, UK). Repetitive electrical pulses (0.5-ms duration at 0.2 Hz) were applied to the tibial or sciatic nerves by an electric stimulator (SEN-3301, Nihon Kohden, Tokyo, Japan) through a stimulus isolator (SS-203J, Nihon Kohden, Tokyo, Japan). For H-reflex recordings, electrical stimuli of graded intensity were applied to nerves for determining the intensity that evokes the maximal amplitude of M response and H-reflex. A total of 25 repetitive stimuli at an intensity that evokes the maximal amplitude were delivered to evoke constant M response and H-reflex responses. The first five responses were discarded to allow reflex stabilization. Latencies of each response and conduction velocity (meters per second) were measured. The maximum amplitude of H-reflex (H_{max}) and M responses (M_{max}) was used to calculate the H_{max}/M_{max} ratio. H-reflex and M response were measured from both hindlimbs. Data of H_{max}/M_{max} ratio and H-reflex latency were excluded when the H-reflex was not evoked.

AAV vector preparation and injection

AAV vectors were prepared by using the AAV Helper Free Expression System (Cell Biolabs Inc., San Diego, CA) as previously described (*77*). We chose AAV9 serotype according to the previous report to deliver exogenous gene to DRG neurons (*40*). The packaging plasmids (pAAV-9 and pHelper) and transfer plasmids (pAAV-CAG-EGFP and pAAV-CAG-Cre) were transfected into human embryonic kidney 293T cells using the calcium phosphate method. A crude cell extract containing AAV vector particles was obtained from transfected cells, and then AAV vector particles were purified by serial ultracentrifugation with cesium chloride. The purified particles were dialyzed with PBS containing 0.001% Pluronic F-68 (Sigma-Aldrich, St. Louis, MO), followed by concentration with an Amicon 10K molecular weight cut-off (MWCO) filter (Merck Millipore, Darmstadt, Germany). The copy number of the vector genomes (vg) was determined by real-time quantitative polymerase chain reaction. AAV9 vectors in PBS (40 μl, 1.0 to 1.4×10^{12} vg/ml) were intraperitoneally administrated into ICR $Dst^{Gt/Gt}$ mice at 1 to 3 days of age using a 31-G thin-walled needle.

Tissue clearing protocol and imaging

The brain and spinal cord were made transparent for imaging according to the improved CUBIC protocol (*78*). The tissues were dissected from mice following perfusion with PBS, pH 7.4, and 4% PFA in 0.1 M PB. The tissues were postfixed overnight in 4% PFA in 0.1 M PB at 4°C and washed with PBS. For 5 days, the samples were immersed in CUBIC-L [10% polyethylene glycol mono-p-isooctyphenyl ether (12969-25, Nacalai Tesque, Kyoto) and 10% *N*-butyldiethanolamine (B0725, Tokyo Chemical Industry, Tokyo) in water] with shake at 37°C. CUBIC-L was exchanged at 2 days after the immersion. The samples were then washed three times with PBS at room temperature for 2 hours and then stained for 5 days at room temperature with rat monoclonal anti-GFP antibody labeled with Alexa Fluor 647 (1:100; D153-A64, MBL) in buffer (0.5% Triton X-100, 0.25% Casein, and 0.01% sodium azide). After staining, the samples were washed three times with PBS at room temperature for 2 hours and postfixed with 1% PFA in 0.1 M PB at room temperature for 5 hours. Samples were immersed in 50% CUBIC-R [45% 2,3-dimethyl-1-phenyl-5-pyrazolone (D1876, Tokyo Chemical Industry) and 30% nicotinamide (N0078, Tokyo Chemical Industry), pH adjusted to approximately 8 to 9 with *N*-butyldiethanolamine (B0725, Tokyo Chemical Industry, Tokyo) in water] diluted in water at room temperature for 5 hours and then gently shaken in CUBIC-R at room temperature overnight. The samples were immersed in new CUBIC-R and kept until the microscopic observation. Fluorescent images were acquired with Light Sheet Fluorescence microscopes (MVX10-LS, Olympus).

Quantification and statistical analysis

VGluT1-positive varicosities were counted in the field of the anterior horn of spinal cord sections with MetaMorph software version 7.10.2. (Molecular Devices, CA, USA). Morphometric analysis was performed on at least three sections per mouse with no blinding. As a statistical analysis, one-way analysis of variance (ANOVA) was performed to compare each group. Statistical analysis was performed using the Easy R (EZR, Saitama Medical Center, Jichi Medical University, Japan) (*79*). Unless otherwise noted, sample size is the number of animals.

Supplementary Materials

The PDF file includes:
Figs. S1 to S14
Legends for movies S1 to S7

Other Supplementary Material for this manuscript includes the following:
Movies S1 to S7

REFERENCES AND NOTES

1. A. Rotthier, J. Baets, V. Timmerman, K. Janssens, Mechanisms of disease in hereditary sensory and autonomic neuropathies. *Nat. Rev. Neurol.* **8**, 73–85 (2012).
2. C. L. Leung, M. Zheng, S. M. Prater, R. K. Liem, The BPAG1 locus: Alternative splicing produces multiple isoforms with distinct cytoskeletal linker domains, including predominant isoforms in neurons and muscles. *J. Cell Biol.* **154**, 691–698 (2001).
3. N. Yoshioka, Roles of dystonin isoforms in the maintenance of neural, muscle, and cutaneous tissues. *Anat. Sci. Int.* **99**, 7–16 (2024).
4. M. Horie, N. Yoshioka, H. Takebayashi, BPAG1 in muscles: Structure and function in skeletal, cardiac and smooth muscle. *Semin. Cell Dev. Biol.* **69**, 26–33 (2017).
5. K. Künzli, B. Favre, M. Chofflon, L. Borradori, One gene but different proteins and diseases: The complexity of dystonin and bullous pemphigoid antigen 1. *Exp. Dermatol.* **25**, 10–16 (2016).
6. A. Lynch-Godrei, R. Kothary, HSAN-VI: A spectrum disorder based on dystonin isoform expression. *Neurol. Genet.* **6**, e389 (2020).
7. S. Edvardson, Y. Cinnamon, C. Jalas, A. Shaag, C. Maayan, F. B. Axelrod, O. Elpeleg, Hereditary sensory autonomic neuropathy caused by a mutation in dystonin. *Ann. Neurol.* **71**, 569–572 (2012).
8. P. Fortugno, F. Angelucci, G. Cestra, L. Camerota, A. S. Ferraro, S. Cordisco, L. Uccioli, D. Castiglia, B. De Angelis, I. Kurth, U. Kornak, F. Brancati, Recessive mutations in the neuronal isoforms of *DST*, encoding dystonin, lead to abnormal actin cytoskeleton organization and HSAN type VI. *Hum. Mutat.* **40**, 106–114 (2019).
9. J.-Y. Jin, P.-F. Wu, J.-Q. He, L.-L. Fan, Z.-Z. Yuan, X.-Y. Pang, J.-Y. Tang, L.-Y. Zhang, Novel compound heterozygous *DST* variants causing hereditary sensory and autonomic neuropathies VI in twins of a Chinese family. *Front. Genet.* **11**, 492 (2020).
10. F. Manganelli, S. Parisi, M. Nolano, F. Tao, S. Paladino, C. Pisciotta, S. Tozza, C. Nesti, A. P. Rebelo, V. Provitera, F. M. Santorelli, M. E. Shy, T. Russo, S. Zuchner, L. Santoro, Novel mutations in *dystonin* provide clues to the pathomechanisms of HSAN-VI. *Neurology* **88**, 2132–2140 (2017).
11. W. W. Motley, S. Züchner, S. S. Scherer, Isoform-specific loss of dystonin causes hereditary motor and sensory neuropathy. *Neurol. Genet.* **6**, e496 (2020).
12. R. P. Sakaria, M. P. Fonville, S. Peravali, P. G. Zaveri, H. J. Mroczkowski, E. Caron, M. F. Weems, A novel variant in the dystonin gene causing hereditary sensory autonomic neuropathy type VI in a male infant: Case report and literature review. *Am. J. Med. Genet. A* **188**, 1245–1250 (2022).
13. L. W. Duchen, S. J. Strich, D. S. Falconer, Clinical and pathological studies of an hereditary neuropathy in mice (*Dystonia musculorum*). *Brain* **87**, 367–378 (1964).
14. A. Brown, G. Bernier, M. Mathieu, J. Rossant, R. Kothary, The mouse *dystonia musculorum* gene is a neural isoform of bullous pemphigoid antigen 1. *Nat. Genet.* **10**, 301–306 (1995).
15. L. Guo, L. Degenstein, J. Dowling, Q. C. Yu, R. Wollmann, B. Perman, E. Fuchs, Gene targeting of *BPAG1*: Abnormalities in mechanical strength and cell migration in stratified epithelia and neurologic degeneration. *Cell* **81**, 233–243 (1995).
16. A. Ferrier, T. Sato, Y. De Repentigny, S. Gibeault, K. Bhanot, R. W. O'Meara, A. Lynch-Godrei, S. F. Kornfeld, K. G. Young, R. Kothary, Transgenic expression of neuronal dystonin isoform 2 partially rescues the disease phenotype of the *dystonia musculorum* mouse model of hereditary sensory autonomic neuropathy VI. *Hum. Mol. Genet.* **23**, 2694–2710 (2014).
17. M. Horie, K. Mekada, H. Sano, Y. Kikkawa, S. Chiken, T. Someya, K. Saito, M. I. Hossain, M. Nameta, K. Abe, K. Sakimura, K. Ono, A. Nambu, A. Yoshiki, H. Takebayashi, Characterization of novel *dystonia musculorum* mutant mice: Implications for central nervous system abnormality. *Neurobiol. Dis.* **96**, 271–283 (2016).
18. Y. De Repentigny, A. Ferrier, S. D. Ryan, T. Sato, R. Kothary, Motor unit abnormalities in *Dystonia musculorum* mice. *PLOS ONE* **6**, e21093 (2011).
19. M. I. Hossain, M. Horie, N. Yoshioka, M. Kurose, K. Yamamura, H. Takebayashi, Motoneuron degeneration in the trigeminal motor nucleus innervating the masseter muscle in *Dystonia musculorum* mice. *Neurochem. Int.* **119**, 159–170 (2018).
20. M. I. Hossain, M. Horie, H. Takebayashi, Reduced proliferation of oligodendrocyte progenitor cells in the postnatal brain of *dystonia musculorum* mice. *Neurochem. Res.* **43**, 101–109 (2018).
21. X. Liu, L. Ma, H. Liu, J. Gan, Y. Xu, T. Zhang, P. Mu, J. Wu, Y. Shi, Y. Zhang, L. Gong, M. He, Cell-type-specific gene inactivation and *in situ* restoration via recombinase-based flipping of targeted genomic region. *J. Neurosci.* **40**, 7169–7186 (2020).
22. F. Schnütgen, S. De-Zolt, P. Van Sloun, M. Hollatz, T. Floss, J. Hansen, J. Altschmied, C. Seisenberger, N. B. Ghyselinck, P. Ruiz, P. Chambon, W. Wurst, H. von Melchner, Genomewide production of multipurpose alleles for the functional analysis of the mouse genome. *Proc. Natl. Acad. Sci. U.S.A.* **102**, 7221–7226 (2005).
23. M. Horie, K. Watanabe, A. K. Bepari, J.-I. Nashimoto, K. Araki, H. Sano, S. Chiken, A. Nambu, K. Ono, K. Ikenaka, A. Kakita, K.-I. Yamamura, H. Takebayashi, Disruption of actin-binding domain-containing Dystonin protein causes *dystonia musculorum* in mice. *Eur. J. Neurosci.* **40**, 3458–3471 (2014).
24. P. S. Danielian, D. Muccino, D. H. Rowitch, S. K. Michael, A. P. McMahon, Modification of gene activity in mouse embryos *in utero* by a tamoxifen-inducible form of Cre recombinase. *Curr. Biol.* **8**, 1323–1326 (1998).
25. P. Dietrich, R. Shanmugasundaram, E. Shuyu, I. Dragatsis, Congenital hydrocephalus associated with abnormal subcommissural organ in mice lacking huntingtin in Wnt1 cell lineages. *Hum. Mol. Genet.* **18**, 142–150 (2009).
26. M. Z. Jackson, K. A. Gruner, C. Qin, W. G. Tourtellotte, A neuron autonomous role for the familial dysautonomia gene ELP1 in sympathetic and sensory target tissue innervation. *Development* **141**, 2452–2461 (2014).
27. N. M. Joseph, Y.-S. Mukouyama, J. T. Mosher, M. Jaegle, S. A. Crone, E.-L. Dormand, K.-F. Lee, D. Meijer, D. J. Anderson, S. J. Morrison, Neural crest stem cells undergo multilineage differentiation in developing peripheral nerves to generate endoneurial fibroblasts in addition to Schwann cells. *Development* **131**, 5599–5612 (2004).
28. F. Seehusen, K. Kiel, S. Jottini, P. Wohlsein, A. Habierski, K. Seibel, T. Vogel, H. Urlaub, M. Kollmar, W. Baumgärtner, U. Teichmann, Axonopathy in the central nervous system is the hallmark of mice with a novel intragenic null mutation of *dystonin*. *Genetics* **204**, 191–203 (2016).

29. N. Yoshioka, M. Kurose, M. Yano, D. M. Tran, S. Okuda, Y. Mori-Ochiai, M. Horie, T. Nagai, I. Nishino, S. Shibata, H. Takebayashi, Isoform-specific mutation in Dystonin-b gene causes late-onset protein aggregate myopathy and cardiomyopathy. *eLife* **11**, e78419 (2022).
30. J. A. Carlsten, R. Kothary, D. E. Wright, Glial cell line-derived neurotrophic factor-responsive and neurotrophin-3-responsive neurons require the cytoskeletal linker protein dystonin for postnatal survival. *J. Comp. Neurol.* **432**, 155–168 (2001).
31. F. J. Alvarez, R. M. Villalba, R. Zerda, S. P. Schneider, Vesicular glutamate transporters in the spinal cord, with special reference to sensory primary afferent synapses. *J. Comp. Neurol.* **472**, 257–280 (2004).
32. A. Takeoka, S. Arber, Functional local proprioceptive feedback circuits initiate and maintain locomotor recovery after spinal cord injury. *Cell Rep.* **27**, 71–85.e3 (2019).
33. S. Zurborg, A. Piszczek, C. Martínez, P. Hublitz, M. Al Banchaabouchi, P. Moreira, E. Perlas, P. A. Heppenstall, Generation and characterization of anAdvillin-Cre driver mouse line. *Mol. Pain* **7**, 1744-8069-7-66 (2011).
34. H. Hasegawa, S. Abbott, B. X. Han, Y. Qi, F. Wang, Analyzing somatosensory axon projections with the sensory neuron-specific *Advillin* gene. *J. Neurosci.* **27**, 14404–14414 (2007).
35. D. V. Hunter, B. D. Smaila, D. M. Lopes, J. Takatoh, F. Denk, M. S. Ramer, Advillin is expressed in all adult neural crest-derived neurons. *eNeuro* **5**, ENEURO.0077-18.2018 (2018).
36. F. Imai, D. R. Ladle, J. R. Leslie, X. Duan, T. A. Rizvi, G. M. Ciraolo, Y. Zheng, Y. Yoshida, Synapse formation in monosynaptic sensory-motor connections is regulated by presynaptic Rho GTPase Cdc42. *J. Neurosci.* **36**, 5724–5735 (2016).
37. X. Zhou, L. Wang, H. Hasegawa, P. Amin, B.-X. Han, S. Kaneko, Y. He, F. Wang, Deletion of PIK3C3/Vps34 in sensory neurons causes rapid neurodegeneration by disrupting the endosomal but not the autophagic pathway. *Proc. Natl. Acad. Sci. U.S.A.* **107**, 9424–9429 (2010).
38. R. A. Kimmel, D. H. Turnbull, V. Blanquet, W. Wurst, C. A. Loomis, A. L. Joyner, Two lineage boundaries coordinate vertebrate apical ectodermal ridge formation. *Genes Dev.* **14**, 1377–1389 (2000).
39. T. Sapir, E. J. Geiman, Z. Wang, T. Velasquez, S. Mitsui, Y. Yoshihara, E. Frank, F. J. Alvarez, M. Goulding, Pax6 and Engrailed 1 regulate two distinct aspects of Renshaw cell development. *J. Neurosci.* **24**, 1255–1264 (2004).
40. A. Machida, H. Kuwahara, A. Mayra, T. Kubodera, T. Hirai, F. Sunaga, M. Tajiri, Y. Hirai, T. Shimada, H. Mizusawa, T. Yokota, Intraperitoneal administration of AAV9-shRNA inhibits target gene expression in the dorsal root ganglia of neonatal mice. *Mol. Pain* **9**, 36 (2013).
41. R. Santos, S. Kawauchi, R. E. Jacobs, M. E. Lopez-Burks, H. Choi, J. Wikenheiser, B. Hallgrimsson, H. A. Jamniczky, S. E. Fraser, A. D. Lander, A. L. Calof, Conditional creation and rescue of *Nipbl*-deficiency in mice reveals multiple determinants of risk for congenital heart defects. *PLOS Biol.* **14**, e2000197 (2016).
42. M. S. Minett, M. A. Nassar, A. K. Clark, G. Passmore, A. H. Dickenson, F. Wang, M. Malcangio, J. N. Wood, Distinct Nav1.7-dependent pain sensations require different sets of sensory and sympathetic neurons. *Nat. Commun.* **3**, 791 (2012).
43. M. Horie, N. Yoshioka, S. Kusumi, H. Sano, M. Kurose, I. Watanabe-Iida, I. Hossain, S. Chiken, M. Abe, K. Yamamura, K. Sakimura, A. Nambu, M. Shibata, H. Takebayashi, Disruption of *dystonin* in Schwann cells results in late-onset neuropathy and sensory ataxia. *Glia* **68**, 2330–2344 (2020).
44. A. Lynch-Godrei, Y. De Repentigny, R. A. Yaworski, S. Gagnon, J. Butcher, J. Manoogian, A. Stintzi, R. Kothary, Characterization of gastrointestinal pathologies in the *dystonia musculorum* mouse model for hereditary sensory and autonomic neuropathy type VI. *Neurogastroenterol. Motil.* **32**, e13773 (2020).
45. K.-W. Tseng, M.-L. Peng, Y.-C. Wen, K.-J. Liu, C.-L. Chien, Neuronal degeneration in autonomic nervous system of *Dystonia musculorum* mice. *J. Biomed. Sci.* **18**, 9 (2011).
46. F. Piguet, C. de Montigny, N. Vaucamps, L. Reutenauer, A. Eisenmann, H. Puccio, Rapid and complete reversal of sensory ataxia by gene therapy in a novel model of friedreich ataxia. *Mol. Ther.* **26**, 1940–1952 (2018).
47. T. Terashima, K. Oka, A. B. Kritz, H. Kojima, A. H. Baker, L. Chan, DRG-targeted helper-dependent adenoviruses mediate selective gene delivery for therapeutic rescue of sensory neuronopathies in mice. *J. Clin. Invest.* **119**, 2100–2112 (2009).
48. J. R. Mendell, S. Al-Zaidy, R. Shell, W. D. Arnold, L. R. Rodino-Klapac, T. W. Prior, L. Lowes, L. Alfano, K. Berry, K. Church, J. T. Kissel, S. Nagendran, J. L'Italien, D. M. Sproule, C. Wells, J. A. Cardenas, M. D. Heitzer, A. Kaspar, S. Corcoran, L. Braun, S. Likhite, C. Miranda, K. Meyer, K. D. Foust, A. H. M. Burghes, B. K. Kaspar, Single-dose gene-replacement therapy for spinal muscular atrophy. *N. Engl. J. Med.* **377**, 1713–1722 (2017).
49. K. M. Nishiguchi, K. Fujita, F. Miya, S. Katayama, T. Nakazawa, Single AAV-mediated mutation replacement genome editing in limited number of photoreceptors restores vision in mice. *Nat. Commun.* **11**, 482 (2020).
50. J. Nishiyama, T. Mikuni, R. Yasuda, Virus-mediated genome editing via homology-directed repair in mitotic and postmitotic cells in mammalian brain. *Neuron* **96**, 755–768.e5 (2017).
51. R. Khalesi, N. Harvey, M. Garshasbi, E. Kalamati, L. Youssefian, H. Vahidnezhad, J. Uitto, Pathogenic *DST* sequence variants result in either epidermolysis bullosa simplex (EBS) or hereditary sensory and autonomic neuropathy type 6 (HSAN-VI). *Exp. Dermatol.* **31**, 949–955 (2022).
52. N. Yoshioka, Y. Kabata, M. Kuriyama, N. Bizen, L. Zhou, D. M. Tran, M. Yano, A. Yoshiki, T. Ushiki, T. J. Sproule, R. Abe, H. Takebayashi, Diverse dystonin gene mutations cause distinct patterns of Dst isoform deficiency and phenotypic heterogeneity in *Dystonia musculorum* mice. *Dis. Model. Mech.* **13**, dmm041608 (2020).
53. C. C. Liang, L. M. Tanabe, S. Jou, F. Chi, W. T. Dauer, TorsinA hypofunction causes abnormal twisting movements and sensorimotor circuit neurodegeneration. *J. Clin. Invest.* **124**, 3080–3092 (2014).
54. S. S. Pappas, K. Darr, S. M. Holley, C. Cepeda, O. S. Mabrouk, J.-M. T. Wong, T. M. LeWitt, R. Paudel, H. Houlden, R. T. Kennedy, M. S. Levine, W. T. Dauer, Forebrain deletion of the dystonia protein torsinA causes dystonic-like movements and loss of striatal cholinergic neurons. *eLife* **4**, e08352 (2015).
55. S. S. Pappas, J. Li, T. M. LeWitt, J. K. Kim, U. R. Monani, W. T. Dauer, A cell autonomous torsinA requirement for cholinergic neuron survival and motor control. *eLife* **7**, e36691 (2018).
56. D. P. Calderon, R. Fremont, F. Kraenzlin, K. Khodakhah, The neural substrates of rapid-onset Dystonia-Parkinsonism. *Nat. Neurosci.* **14**, 357–365 (2011).
57. C. E. Pizoli, H. A. Jinnah, M. L. Billingsley, E. J. Hess, Abnormal cerebellar signaling induces dystonia in mice. *J. Neurosci.* **22**, 7825–7833 (2002).
58. J. J. White, R. V. Sillitoe, Genetic silencing of olivocerebellar synapses causes dystonia-like behaviour in mice. *Nat. Commun.* **8**, 14912 (2017).
59. R. Fremont, A. Tewari, C. Angueyra, K. Khodakhah, A role for cerebellum in the hereditary dystonia DYT1. *eLife* **6**, e22775 (2017).
60. J. Zhang, J. A. P. Weinrich, J. B. Russ, J. D. Comer, P. K. Bommareddy, R. J. DiCasoli, C. V. E. Wright, Y. Li, P. J. van Roessel, J. A. Kaltschmidt, A role for dystonia-associated genes in spinal GABAergic interneuron circuitry. *Cell Rep.* **21**, 666–678 (2017).
61. X. J. Chen, E. N. Levedakou, K. J. Millen, R. L. Wollmann, B. Soliven, B. Popko, Proprioceptive sensory neuropathy in mice with a mutation in the cytoplasmic Dynein heavy chain 1 gene. *J. Neurosci.* **27**, 14515–14524 (2007).
62. R. Klein, I. Silos-Santiago, R. J. Smeyne, S. A. Lira, R. Brambilla, S. Bryant, L. Zhang, W. D. Snider, M. Barbacid, Disruption of the neurotrophin-3 receptor gene trkC eliminates la muscle afferents and results in abnormal movements. *Nature* **368**, 249–251 (1994).
63. D. Levanon, D. Bettoun, C. Harris-Cerruti, E. Woolf, V. Negreanu, R. Eilam, Y. Bernstein, D. Goldenberg, C. Xiao, M. Fliegauf, E. Kremer, F. Otto, O. Brenner, A. Lev-Tov, Y. Groner, The Runx3 transcription factor regulates development and survival of TrkC dorsal root ganglia neurons. *EMBO J.* **21**, 3454–3463 (2002).
64. S. H. Woo, V. Lukacs, J. C. de Nooij, D. Zaytseva, C. R. Criddle, A. Francisco, T. M. Jessell, K. A. Wilkinson, A. Patapoutian, Piezo2 is the principal mechanotransduction channel for proprioception. *Nat. Neurosci.* **18**, 1756–1762 (2015).
65. A. M. Pocratsky, F. Nascimento, M. G. Özyurt, I. J. White, R. Sullivan, B. J. O'Callaghan, C. C. Smith, S. Surana, M. Beato, R. M. Brownstone, Pathophysiology of Dyt1-*Tor1a* dystonia in mice is mediated by spinal neural circuit dysfunction. *Sci. Transl. Med.* **15**, eadg3904 (2023).
66. R. Berlot, K. P. Bhatia, M. Kojović, Pseudodystonia: A new perspective on an old phenomenon. *Parkinsonism Relat. Disord.* **62**, 44–50 (2019).
67. H. Takebayashi, S. Yoshida, M. Sugimori, H. Kosako, R. Kominami, M. Nakafuku, Y.-I. Nabeshima, Dynamic expression of basic helix-loop-helix Olig family members: Implication of Olig2 in neuron and oligodendrocyte differentiation and identification of a new member, Olig3. *Mech. Dev.* **99**, 143–148 (2000).
68. T. D. Singh, K. Mizuno, T. Kohno, S. Nakamura, BDNF and trkB mRNA expression in neurons of the neonatal mouse barrel field cortex: Normal development and plasticity after cauterizing facial vibrissae. *Neurochem. Res.* **22**, 791–797 (1997).
69. K. Ono, H. Takebayashi, K. Ikeda, M. Furusho, T. Nishizawa, K. Watanabe, K. Ikenaka, Regional- and temporal-dependent changes in the differentiation of Olig2 progenitors in the forebrain, and the impact on astrocyte development in the dorsal pallium. *Dev. Biol.* **320**, 456–468 (2008).
70. K. Watanabe, N. Tamamaki, T. Furuta, S. L. Ackerman, K. Ikenaka, K. Ono, Dorsally derived netrin 1 provides an inhibitory cue and elaborates the 'waiting period' for primary sensory axons in the developing spinal cord. *Development* **133**, 1379–1387 (2006).
71. D. Goryunov, A. Adebola, J. J. Jefferson, C. L. Leung, A. Messer, R. K. H. Liem, Molecular characterization of the genetic lesion in *Dystonia musculorum* (*dt-Alb*) mice. *Brain Res.* **1140**, 179–187 (2007).
72. L. Zhou, M. I. Hossain, M. Yamazaki, M. Abe, R. Natsume, K. Konno, S. Kageyama, M. Komatsu, M. Watanabe, K. Sakimura, H. Takebayashi, Deletion of exons encoding carboxypeptidase domain of Nna1 results in Purkinje cell degeneration (*pcd*) phenotype. *J. Neurochem.* **147**, 557–572 (2018).
73. S. Chiken, P. Shashidharan, A. Nambu, Cortically evoked long-lasting inhibition of pallidal neurons in a transgenic mouse model of dystonia. *J. Neurosci.* **28**, 13967–13977 (2008).

74. H. Sano, S. Chiken, T. Hikida, K. Kobayashi, A. Nambu, Signals through the striatopallidal *Indirect* pathway stop movements by phasic excitation in the substantia nigra. *J. Neurosci.* **33**, 7583–7594 (2013).
75. R. Jeffrey-Gauthier, M. Piché, H. Leblond, H-reflex disinhibition by lumbar muscle inflammation in a mouse model of spinal cord injury. *Neurosci. Lett.* **690**, 36–41 (2019).
76. A. Schulz, C. Walther, H. Morrison, R. Bauer, *In vivo* electrophysiological measurements on mouse sciatic nerves. *J. Vis. Exp.* **86**, 51181 (2014).
77. H. Sano, K. Kobayashi, N. Yoshioka, H. Takebayashi, A. Nambu, Retrograde gene transfer into neural pathways mediated by adeno-associated virus (AAV)-AAV receptor interaction. *J. Neurosci. Methods* **345**, 108887 (2020).
78. K. Tainaka, T. C. Murakami, E. A. Susaki, C. Shimizu, R. Saito, K. Takahashi, A. Hayashi-Takagi, H. Sekiya, Y. Arima, S. Nojima, M. Ikemura, T. Ushiku, Y. Shimizu, M. Murakami, K. F. Tanaka, M. Iino, H. Kasai, T. Sasaoka, K. Kobayashi, K. Miyazono, E. Morii, T. Isa, M. Fukayama, A. Kakita, H. R. Ueda, Chemical landscape for tissue clearing based on hydrophilic reagents. *Cell Rep.* **24**, 2196–2210.e9 (2018).
79. Y. Kanda, Investigation of the freely available easy-to-use software 'EZR' for medical statistics. *Bone Marrow Transplant.* **48**, 452–458 (2013).

Acknowledgments: We thank A. McMahon and A. Ohazama for *Wnt1-Cre* mice, F. Wang and H. Hasegawa for *Avil-Cre* mice, A. Joyner and M. Hoshino for *En1-Cre* mice, R. K. Liem for anti-Dst antibody, S. Nakamura for *TrkB* plasmid, and K. Abe for *TrkA* and *TrkC* plasmids. In addition, we thank M. Horie, N. Bizen, and M. Yano for the discussion and L. Zhou, Y. Mori-Ochiai, Y. Imada, S. Yamagiwa, S. Takahashi, T. Watanabe, and K. Nakajima for technical assistance. We thank J. Allen from Edanz for editing a draft of this manuscript. **Funding:** This project was funded by grants from JSPS (18H02592 and 21H02652 to H.T., 20K15912 and 23K06317 to N.Y., and 19KK0193, 23H02594, and 23H04688 to A.N.), Grant-in-Aid for Scientific Research on Innovative Areas, "Non-linear Neuro-oscillology" (18H04939 to H.T. and 15H05873 to A.N.), grants from Japan Agency for Medical Research and Development (AMED) (JP18dm0307005 and JP21dm0207115 to A.N. and JP21wm0425001 and JP21zf0127004 to K.T.), grants from the Cooperative Study Programs of National Institute for Physiological Sciences and Center for Animal Resources and Collaborative Study of NINS (H.T., N.Y., A.N., K.K., and S.C.), the Uehara Memorial Foundation (H.T.), Nagai Promotion Foundation for Science of Perception (H.T.), Setsuro Fujii Memorial the Osaka Foundation for Promotion of Fundamental Medical Research (N.Y.), The Nakatomi Foundation (N.Y.), Union Tool Scholarship Foundation (N.Y.), Yamaguchi Educational and Scholarship Foundation (N.Y.), The Nakatani Foundation (N.Y.), Nippon Shinyaku (N.Y.), Takeda Science Foundation (N.Y.), Niigata University U-go Grant (N.Y.), and a grant for Interdisciplinary Joint Research Project from Brain Research Institute from Niigata University (H.T.). **Author contributions:** Conceptualization: N.Y., M.K., and H.T. Methodology: N.Y., M.K., S.C., K.T., A.N., and H.T. Investigation: N.Y., M.K., H.S., D.M.T., S.C., K.T., and H.T. Formal analysis: N.Y., M.K., H.S., S.C., and A.N. Visualization: N.Y., M.K., S.C., A.N., and H.T. Project administration: N.Y., M.K., and H.T. Supervision: M.K. and H.T. Funding acquisition: N.Y., K.T., A.N., and H.T. Writing—original draft: N.Y., M.K., A.N., and H.T. Writing—review and editing: N.Y., M.K., S.C., K.T., K.Y., K.K., A.N., and H.T. Validation: N.Y., M.K., K.Y., and H.T. Data curation: N.Y. and H.T. Resources: M.K., K.T., K.K., and H.T. Software: S.C. and A.N. **Competing interests:** K.T. has filed a patent application for CUBIC reagents. The other authors declare that they have no competing interests. **Data and materials availability:** All data needed to evaluate the conclusions in the paper are present in the paper and/or the Supplementary Materials. This study includes no dataset deposited in external repositories. The *Avil-Cre* mouse can be provided by F. Wang pending scientific review and a completed material transfer agreement. Requests for the *Avil-Cre* mouse can be submitted to RIKEN BRC. The *En1-Cre* mouse can be provided by the Jackson Laboratory pending scientific review and a completed material transfer agreement. Requests for the *En1-Cre* mouse should be submitted to the Jackson Laboratory.

Submitted 24 September 2023
Accepted 25 June 2024
Published 26 July 2024
10.1126/sciadv.adj9335